An Investigation of the Optical Properties of Metal Nanoparticles for the Application in a Diffuse Light Solar Cell

Mirjam Dyrhovden Fjell

Master Thesis in Energy

Supervisors:
Professor Dr. Bodil Holst
Dr. Martin Møller Greve

Faculty of Mathematics and Natural Science
University of Bergen

June 2020

Abstract

The need of renewable energy is increasing as the global energy demand increases concurrently with greenhouse gas emissions from energy use. According to the International Energy Agency, the energy demand will rise by 1.3 % every year to 2040, and more and more energy will be delivered from electricity. The electrical power sector is the single largest source of carbon emissions, hence the share of renewables in the electricity generation needs to be increased. Photovoltaic solar cells convert solar radiation directly into electricity and are expected to play an important role in the electricity production in the coming years. However, the efficiency of today's commercial silicon solar cells, which dominate the solar cell installations today, is only about 20 % and is highly dependent on the intensity of the incoming solar radiation. Under diffuse light conditions, the intensity of the incoming solar radiation is decreased, and efficient light incoupling is therefore of paramount importance to make solar cells an alternative in areas where diffuse light conditions dominate. In this thesis work, sustainable solutions using plasmonic metal nanoparticles to increase the light incoupling in silicon solar cells over a broad angular range, corresponding to diffuse light conditions, have been investigated. Through numerical simulations using an FDTD solver, it has been found that the introduction of spherical aluminum nanoparticles with a 3 nm oxide layer of diameter 120 nm in a periodic array with period 360 nm on top of flat silicon solar cells can enhance the transmission of light by 7.46 % over all incident light angles. This leads to an overall increase in the solar cell efficiency of 1.71 %, or a relative increase of 7.23 %. Aluminum is the 7th most abundant material on Earth and also cheap with respect to material price, making it realistic that it can be used in large scale solar cell production.

Acknowledgement

First, I wish to thank my supervisors Professor Dr. Bodil Holst and Dr. Martin Møller Greve for their support, guidance and constructive feedback throughout the work with this thesis. I also wish to thank the Halas Research Group at Rice University for welcoming me and including me in their group while I was there. The guidance, discussions and constructive feedback they gave me during my stay was invaluable. I would like to thank Hordaland Fylkeskommune (now part of Vestland Fylke) and the L. Meltzers Høyskolefond for their financial grants. Without these, the exchange trip to Rice University would not have been possible. Due to the outbreak of the COVID-19 pandemic I had to terminate the stay at Rice University four weeks earlier than planned, as the Norwegian government recommended Norwegian citizens abroad to return home. I wish to thank UiB for their help in conjunction with the travel home. Finally, I would like to give thanks to my family for their love and support, and last, but not least, I wish to thank my husband for his support and for always having faith in me.

Contents

List of Figures

List of Tables

Chapter 1

Introduction

1.1 The Need of Renewable Energy Sources For Electricity Production

The life on Earth relies on the greenhouse effect. Due to gases in the Earth's atmosphere, longwave radiation from the surface of the Earth is absorbed and reemitted in all directions, making the surface of the Earth and the lower atmosphere warmer [1]. The most important greenhouse gases are water vapor (H_2O), carbon dioxide (CO_2), methane (CH_4) and nitrous oxides (NO_x) [1]. Since the industrial revolution starting in the late 18th century, there has been an increase in emission of greenhouse gases, especially CO_2, as a result of fossil fuel combustion. The fifth Intergovernmental Panel on Climate Change (IPCC) report (2013) [2] clearly states that this increase is due to anthropogenic activities. The report further states that due to the continued emissions of greenhouse gases, the global surface temperature is increasing. This temperature rise has many negative consequences, such as sea-level rise, melting of sea ice in the Arctic and change in the global water cycle.

Concurrently, the world's energy demand is growing. According to the BP Statistical Review of World Energy 2019 [3], the global world consumption was 580 EJ (10^{18} J) in 2018, a growth of 2.9 % compared to 2017. The energy demand is expected to continue to grow by 1.3 % every year to 2040 according to the IEA World Energy Outlook 2019 [4]. As the energy use is growing, so are the carbon emissions from energy use. The electrical power sector plays a significant role in this growth as it is the single largest source of carbon emissions, and the electricity demand is expected to grow. According to the Energy Transition Outlook 2019 from DNV-GL [5], the share of energy delivered from electricity will increase from 19 % in 2017 to 40 % in 2050. One of the main reasons for this is the transition from combustion vehicles to electrical vehicles. By 2032 it is expected that 50 % of new passenger cars sold are electrical. The transport sector accounts for 28 % of the global energy demand today, and it is expected that the share will stay approximately the same in 2050. Road transport accounts for 80 % of the energy demand in the transport sector [5].

As can be seen in fig. 1.1, coal has dominated as fuel for electrical power generation

over the last 33 years, its share being stable at around 40 % (38 % in 2018). The share of renewables, excluding hydroelectricity, is increasing. However, to reach the goal in the Paris Agreement article 2.1.a) on "Holding the increase in the global average temperature to well below 2 °C above pre-industrial levels and pursuing efforts to limit the temperature increase to 1.5 °C above pre-industrial levels" [6], the emissions of CO_2 needs to be reduced by as much as approximately 68 % by 2050 according to the IEA World Energy Outlook 2019 [4]. One way towards this goal is to reduce the emissions from the electrical power sector by increasing the share of renewables in the global electrical power generation.

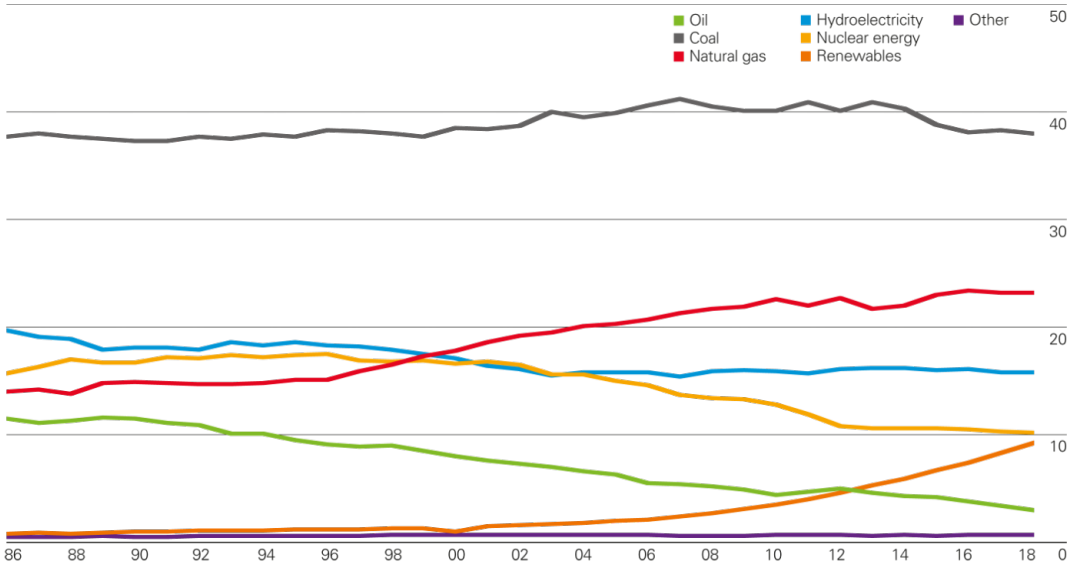

Figure 1.1: The global electricity generation by fuel given in percentage. Coal accounts for 38 % of the electricity generation, making it the dominant fuel. Renewables (including hydroelectricity) accounts for 25 % of the global electricity generation [3].

The Sun is a large source of renewable energy. Every second, 173 000 000 GJ of energy enters the atmosphere of the Earth from the Sun. Compared to the rate at which humans use energy, this is more than 10 000 times more energy, meaning that if only 0.01 % of the energy from the Sun could be used, it would be sufficient to run today's entire society (2018) [7]. One way to harvest the energy from the Sun is to use photovoltaic (PV) solar cells. PV cells convert solar radiation directly into electricity, and in the 1950s, the first practical PV cells were developed [7]. They were made from silicon (Si) and were both expensive and inefficient. Therefore, their field of application was very narrow. Since then, the PV cell technology has been highly developed, making them cheaper and more efficient. In some areas, PV cells are competitive with traditional non-renewable electric power sources [7]. Global installed PV cell capacity was more than 512.3 GW by the end of 2018, providing almost 3 % of the global electricity demand [8]. Crystalline Si technologies dominate the PV cell installations today and account for more than 97 % of the PV cell production (2018) [8]. The PV cell technology is described in detail in chapter 2.

The work in this thesis focuses on how to make PV cells more efficient under diffuse light conditions. PV cells have become cheaper in recent years and the module and installation costs are mainly determining the price of a PV cell. It is therefore necessary to increase the efficiency of the cell to further decrease the price per kWh [9].

1.2 The Diffuse Light Problem for Solar Cells

The product of the voltage and current of a PV cell equals its power output. As will be described in section 2.1.3, PV cells have a maximum voltage (open-circuit voltage) and a maximum current (short-circuit current), and to obtain the maximum power output from the cell it should be operated right below the maximum voltage and current. However, when the insolation is reduced, that is, the solar radiation that reaches the PV cell surface, the maximum voltage and especially maximum current is reduced as well. Consequently, this also reduces the maximum power output from the cell [10].

Fig. 1.2 shows the direct and diffuse insolation on Earth. The diffuse light intensity is much lower than the direct light intensity, making the power output from PV cells under diffuse light conditions low compared to the output under direct light conditions. In addition, a smaller part of the diffuse light is absorbed because it hits the PV cell over a broad angular range, so that the antireflection coating is less effective, as will be further elucidated in section 1.4.2. To make PV cell technology an alternative in areas with little direct light it is of paramount importance to increase the amount of diffuse light absorbed by the cell.

1.3 The Norwegian Situation - PV Cell Perspective

In Norway, the total installed PV cell capacity is 67 MW (end of 2018) [8]. For comparison, the installed hydropower capacity was 32,671 MW in the beginning of 2020, several orders of magnitude higher [12]. One explanation is the weather conditions in Norway which, especially on the west coast, are cloudy and rainy. In Bergen, the largest city on the west coast, it has rained 200 days per year on average over the last 30 years [13]. Thus, it is important to increase the efficiency of PV cells under diffuse light conditions to make them a reasonable alternative in Norway and areas with similar weather conditions.

As explained in the previous section, the maximum power output from a PV cell is obtained when the cell is operated right below the maximum voltage and current, termed the open-circuit voltage and short-circuit current. Both of these depend on the insolation, but also on the cell temperature. The open-circuit voltage decreases as the temperature increases, making the maximum power output smaller [10]. The climate in Norway is cold, and with its long days during summer the operation conditions for PV cells are good [8].

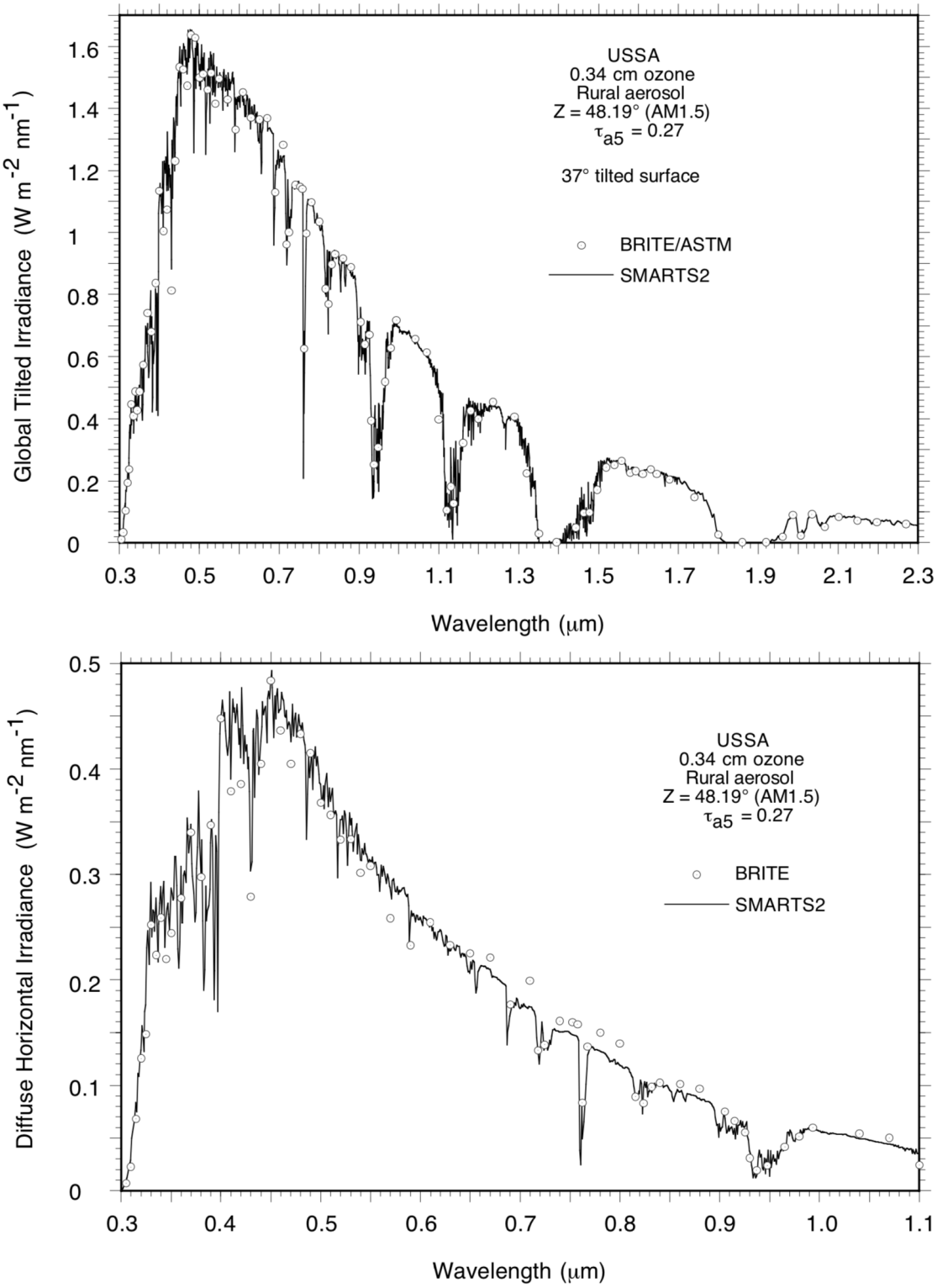

Figure 1.2: Top: The AM1.5 reference spectra for the direct irradiance on Earth. Bottom: The diffuse irradiance on a horizontal surface. The intensity is lower for the diffuse irradiance than for the direct irradiance. Figures are taken from [11].

1.4 How to Solve the Diffuse Light Problem: State of the Art

For a PV cell to perform well, it is of key importance that the PV cell material absorbs as much of the incoming light as possible to generate electron-hole pairs, as will be described in detail in chapter 2. Optical losses due to reflection from the back electrode, shadowing by the front electrodes and reflection from the top surface, as illustrated in fig. 1.3, limits the absorption of the incoming light [10]. In addition, a large portion of the incoming light is lost due to a spectral mismatch between the solar spectrum and the spectral absorption range of the PV cell material [14]. To minimize the reflection from commercial Si PV cells, their surface is textured and coated with an anti reflection coating (ARC) [15]. In recent years, the use of plasmonic structures to increase the light trapping of PV cells has been studied. These technologies will be further elucidated in the following sections.

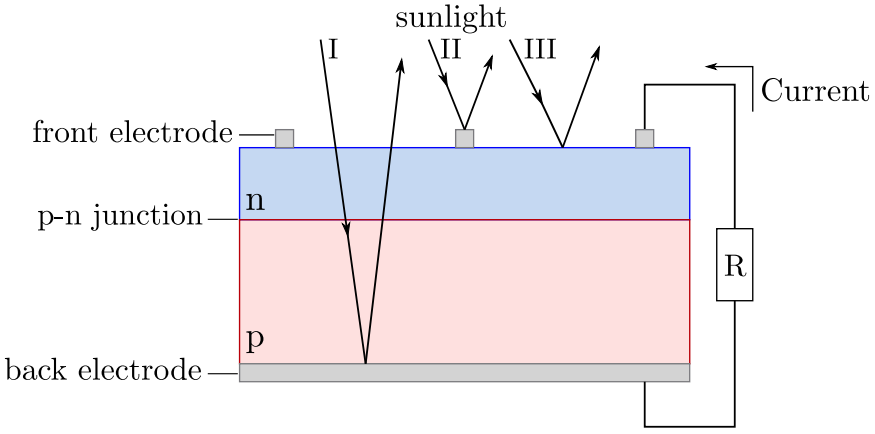

Figure 1.3: A cross section of a single junction PV cell, see section 2.1 for a detailed explanation. The three types of optical losses are shown. (I) losses due to reflection from the back electrode, (II) losses due to shadowing by the front electrodes and (III) losses due to reflection from the top surface [10].

1.4.1 Surface Texturing

Since the mid-70s, the surface of commercial Si PV cells has been textured to decrease its reflectivity [16]. To make the textures, (1 0 0) oriented mono-crystalline Si wafers are chemically etched using anisotropic solutions, typically potassium hydroxide (KOH) or tetramethylammonium hydroxide (TMAH) [17, 18]. By choosing etchants of high selectivity, the etch rate in the $\langle 1\ 0\ 0 \rangle$ direction is much higher than that in the $\langle 1\ 1\ 1 \rangle$ direction. The etching then results in square-based pyramids where the faces are formed by the $\{1\ 1\ 1\}$ planes of the Si crystal [19, 20]. The base angle of these pyramids is 54.7° [18]. Chemical etching could also be used to form inverted pyramids [19]. The goal with texturing PV cells is to direct the light that is reflected off of the textured surface towards the cell at some other place, as illustrated in fig. 1.4.

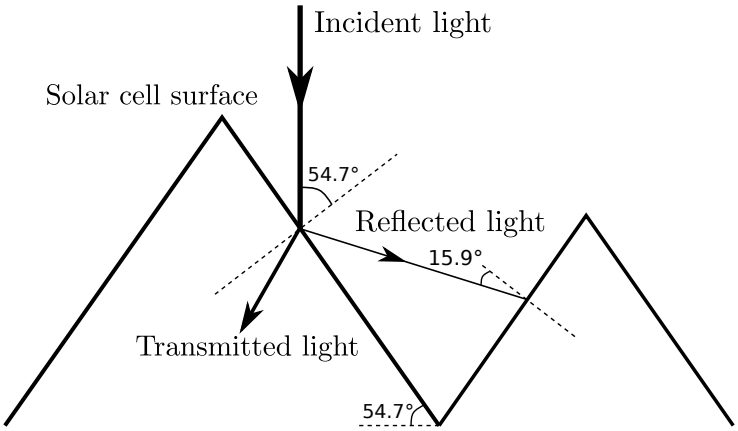

Figure 1.4: Illustration of light reflecting from a pyramidal textured surface. Light that is reflected hits the surface at some other place and could be transmitted there.

1.4.2 Antireflection Coatings

An ARC is a thin film of a dielectric material that is deposited on top of the PV cell to reduce reflection from its front surface [21]. The characteristics of the ARC depends on the refractive index n of the dielectric and the thickness d of the film. The fraction of light that is reflected is given by the Fresnel equations, which depend on the refractive indices of the materials at the interfaces [22, 23]. When the refractive index of the ARC film is equal to the geometric mean of the materials it is interposed between, the suppression of reflection is maximized. The thickness of the film is chosen so that the light reflected from the top of the ARC is out of phase with the light reflected from the bottom of the ARC, resulting in destructive interference, as illustrated in fig. 1.5. The thickness d of the ARC should be a quarter of the wavelength of light in the coating, $\lambda = \lambda_0/n$, where λ_0 is the wavelength in air. Thus, the thickness should be

$$d = \frac{\lambda}{4} = \frac{\lambda_0}{4n} \tag{1.1}$$

The solar spectrum includes more than one wavelength and λ_0 must be selected, preferably close to where the spectrum peaks, at approximately 600 nm (see fig. 1.2). On Si PV cells, titanium dioxide (TiO_2) or silicon nitride (SiN_x) films are typically used as ARCs. The industrial standard for ARCs on crystalline-Si PV cells is SiN_x films deposited with plasma-enhanced chemical vapor deposition (PECVD) [22]. The ARC on the PV cells used in this thesis is deposited in this way.

The reflection properties of the ARC films are both wavelength and angle dependent [24]. The thickness of the ARC films is designed so that they are most effective at wavelengths around 600 nm, as mentioned. However, a large portion of the incident solar radiation has other wavelengths (see fig. 1.2), where the ARC films are less efficient. In addition, destructive interference only occurs when the incident light is at, or close to, normal incidence [22].

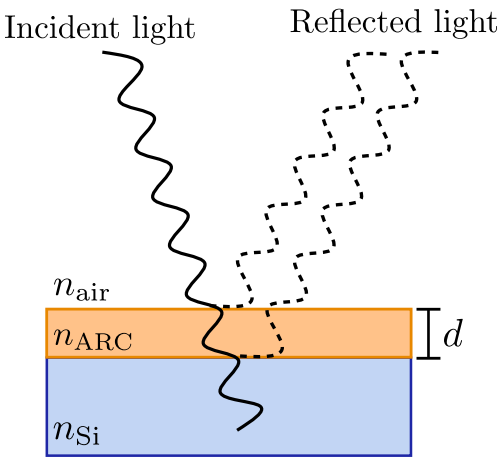

Figure 1.5: An illustration of the destructive interference of light reflected from the air-ARC interface and the ARC-Si interface.

It is not only the destructive interference that relies on the injection angle of the incident light. The reflectance from a silicon nitride (Si_3N_4) surface in air as a function of injection angle is illustrated in fig. 1.6. The reflectance is approximately constant for small angles, while for angles steeper than 50° the reflectance increases rapidly [25].

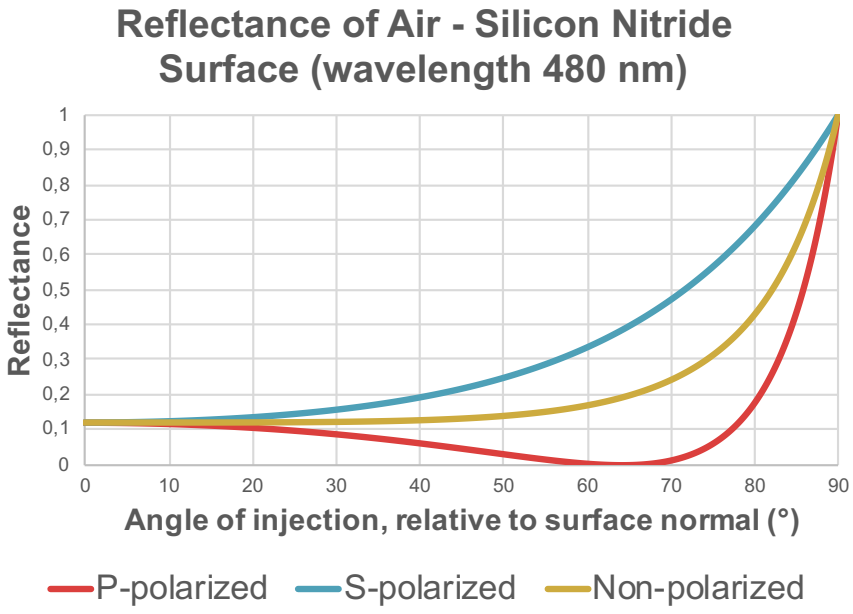

Figure 1.6: The reflectance of an air - Si_3N_4 surface as a function of incident light angle relative to the surface normal. For non-polarized light (yellow curve), the reflectance is approximately constant up to 50°, whereafter it increases rapidly [25].

1.4.3 Plasmonic Solar Cells

The use of plasmonic nanoparticles to increase the efficiency of PV cells has been studied in recent years and could be an additional factor to the conventional solutions described in the previous sections. By exploiting the capability of plasmonic nanoparticles to scatter and enhance the incident light beam within specific spectral regions, tuned by the size, shape, surrounding medium and distribution of the nanoparticles, the energy harvest of the PV cell can be improved [14]. The theory of plasmonics is discussed in chapter 2. Here, a brief overview of work related to PV cells is presented.

Catchpole and Polman [26] showed that cylindrical and hemispherical nanoparticles placed on top of a Si PV cell can increase the path length of light into the cell due to enhanced near-field coupling. Through numerical simulations, they compared silver (Ag) and gold (Au) nanoparticles and found that Ag nanoparticles give the most effective path length enhancement. The enhancement is very size dependent, and 100 nm in diameter Ag hemispheres gave the best result with a path length enhancement of 28 at wavelength 800 nm.

Aluminum (Al) is both an abundant and low-cost metal, making it an interesting alternative to Ag or Au for the use in plasmonic PV cells. The light incoupling of Al nanoparticles located on top of Si PV cells was studied both numerically and experimentally by Zhang et al. [27]. Through simulations, they found that spherical Al nanoparticles incouple light more effectively than both hemispheres and cubes. At longer wavelengths (600 to 1100 nm) the transmission into Si with the addition of spherical Al nanoparticles is reduced compare to the bare Si, which is attributed to a red-shift in the Fano resonance. The optimized enhancement of light transmitted into the PV cell was found for spherical Al nanoparticles of size 150 nm in diameter and surface coverage of 30 %. Experimentally, they measured the photocurrent of the PV cell with and without Al nanoparticles. This time they included a SiN_x layer on top of the cell. With a 20 nm thick SiN_x layer with Al nanoparticles of size 100 nm on average on top, the photocurrent enhancement was 8 %.

Recently, Yu et al. [28] found that the scattering from metal nanoparticles with a dielectric shell, often referred to as core-shell nanoparticles, located on top of a Si substrate is suppressed backward and enhanced forward, thus increasing the optical path length in the Si substrate. Both electric and magnetic resonances can be simultaneously supported by core-shell nanoparticles, making it possible to achieve azimuthally symmetric unidirectional scattering. The particles used by Yu et al. had an Ag core (80-120 nm in diameter) and a dielectric shell where they varied the thickness and refractive index. They found that the maximum optical path length enhancement can be as high as 3133 and the fraction of light scattered into the substrate as high as 0.999, making the application of core-shell nanoparticles particularly useful in thin film PV cells.

1.5 Thesis Objectives

The objective of this thesis work has been to improve the efficiency of commercial Si PV cells under diffuse light conditions by introducing plasmonic nanoparticles on top of the PV cells, and thereby increase the transmission of light into the PV cells. It has all the way been important to find a sustainable solution, both considering the abundance of the materials used as well as the cost. The thesis objectives are

- To determine an appropriate material for the plasmonic nanoparticles, both regarding the light incoupling properties of the material and the price and abundance of it,
- To simulate the transmission of light into a commercial structured Si PV cell under angled illumination, corresponding to diffuse light conditions, when introducing nanoparticles on top of the cell. For simplicity, the substrate was changed to a flat Si PV cell instead of a structured one. The nanoparticle size and distribution should be varied to find the optimal configuration for light incoupling,
- To make a model to calculate the overall efficiency of the Si PV cell based on the transmission results from the simulations,
- To experimentally verify the simulation results at Rice University, Texas, USA, by applying chemically synthesized nanoparticles, with parameters closely matching the simulation results, systematically to a standard ARC coated Si PV cell. This could not be completed due to the outbreak of the COVID-19 pandemic.

1.6 Thesis Outline

In chapter 2, the theoretical background of PV cells and plasmonics is explained, as well as the theory behind the simulation software used in the thesis. Chapter 3 presents the simulation setup and the experimental equipment and setup used. An explanation of the experiments that were planned to do at Rice University, but could not be performed due to the outbreak of the COVID-19 pandemic, is also presented here. The simulation results and efficiency calculations are presented and discussed in chapter 4, while experimental results are presented and discussed in chapter 5. The thesis conclusion and suggestions for future work are given in chapter 6.

Chapter 2

Theory

This chapter presents the theoretical background of this master thesis work. First, the fundamentals of commercial silicon solar cells are described. Then, a brief introduction to the field of plasmonics is given, and finally, the theory behind the simulation software that will be used in this thesis is presented.

2.1 Photovoltaic Solar Cells

The photovoltaic (PV) solar cell technology has evolved a lot since the first PV cell devices in the 1950s, with now both 2nd, 3rd and 4th generation PV cells. In this master thesis, standard (mono)crystalline silicon (Si) PV cells are used, and the focus will therefore be on these. PV cells convert solar radiation directly into electrical energy. Today's commercial PV cells, including crystalline Si PV cells, consist of doped semiconductors in a p-n junction, coupled to an external circuit [7]. This section will first describe the fundamentals of semiconductors and the p-n junction, before the working principle of PV cells is explained, and finally, some characteristics of PV cells are elucidated.

2.1.1 Semiconductors and the p-n junction

When looking at an isolated atom, its electrons have discrete energy levels, also called states. The electrons fill up successively higher energy levels until the atom is neutral, in accordance with the Pauli exclusion principle. The same principle applies to neutral bulk materials. However, in bulk materials, such as crystals, the energy levels of the individual atoms split into closely spaced separate energy levels. This forms continuous energy bands that are separated by so-called bandgaps [7, 29]. The two lowest bands are known as the valence band (VB) and the conduction band (CB). The difference in energy between the top of the VB and the bottom of the CB is called the energy of the bandgap, E_{gap}, as depicted in fig. 2.2. At zero temperature, T = 0 K, the electrons fill all states up to some maximum energy, termed the *Fermi energy*, and none of the above states. At finite temperatures, electrons may be excited into higher energy levels. The probability of an energy level to be occupied is described by the Fermi-Dirac distribution, shown in

fig. 2.1, and given as

$$p(E) = \frac{1}{1 + e^{(E - E_F(T))/k_B T}} \tag{2.1}$$

Here, k_B is the Boltzmann constant, T is the temperature in Kelvin, E is the energy of the state where an electron is found and $E_F(T)$ is the *Fermi level*, that is, the energy where the probability is 1/2. The Fermi level and the Fermi energy are equal at zero temperature [7].

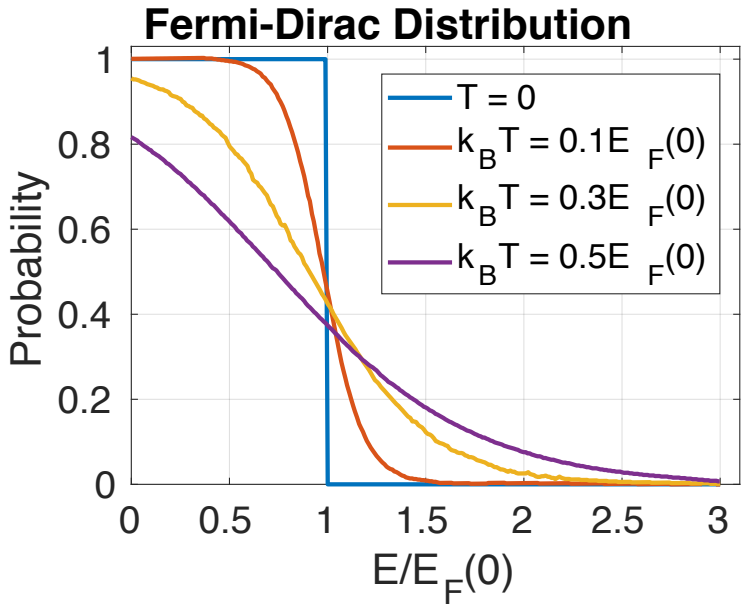

Figure 2.1: The Fermi-Dirac distribution for different temperatures. At room temperature, $k_B T/E_F \approxeq 0.023$ for Si. Figure is reproduced from [7].

The position of the Fermi energy determines whether a material is a metal, a semiconductor or an insulator. As can be seen in fig. 2.2 a), the Fermi energy in a metal is inside a band, and the electrons do not need much energy to be excited to higher energy levels. Therefore, metals are excellent conductors. In a semiconductor and an insulator (fig. 2.2 b) and c)), the Fermi energy lies between the VB and the CB. At zero temperature, the VB is filled while the CB is empty. If the separation between the bands is not too large, electrons may have enough energy to be excited into the CB at room temperature and the material is a reasonable conductor, that is, a *semiconductor*. If the separation between the bands is large, it is very difficult for the electrons to be excited across the bandgap into the CB, and the material is an insulator [7].

The bandgap in real materials can be direct or indirect. A direct bandgap means that the highest energy of the VB has the same momentum as the lowest energy of the CB, as shown in fig. 2.3 a). In fig. 2.3 b), the momenta are different, and the bandgap is said to be indirect. This is the case in for example Si. For an electron to be excited across the bandgap, both momentum and energy have to be conserved. If an electron is excited

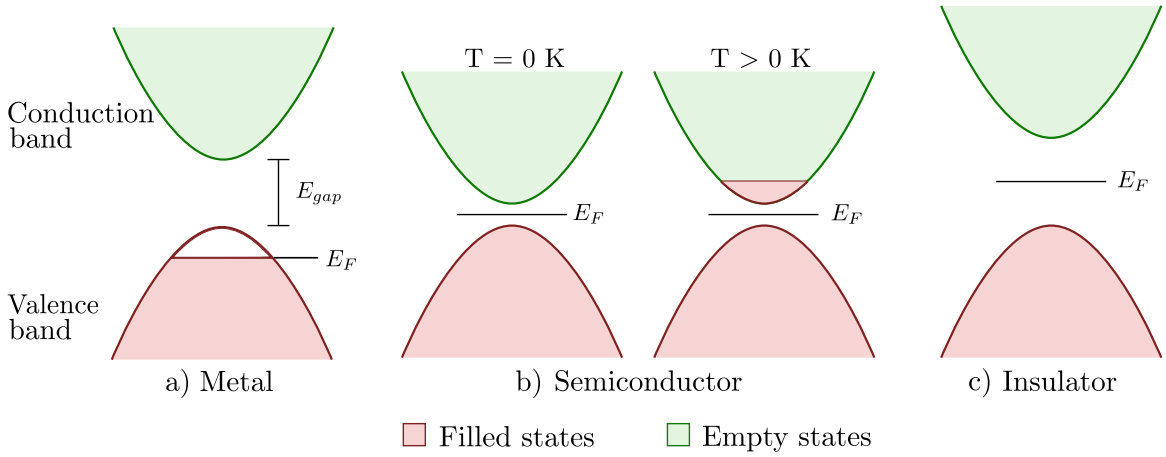

Figure 2.2: An illustration of the energy bands, bandgap and Fermi level in different materials. a) shows a metal, where the Fermi level is located inside an energy band. b) shows a semiconductor at T = 0 K and at T > 0 K. The Fermi level is located between the energy bands. Because the bandgap is small, electrons may be excited across the bandgap into the CB at finite temperatures. In c), the bandgap is too large for electrons to be excited across the bandgap, and the material is an insulator [7].

by a photon with the same energy as the bandgap (or higher energy), energy will be conserved. However, the momentum transferred to an electron from an incoming photon is negligibly small at optical wavelengths, and photons can therefore only excite electrons to a state with the same momentum. Thus, a photon alone cannot excite an electron in a material with an indirect bandgap [30]. Therefore, in an intrinsic (pure) semiconductor with indirect bandgap electrons are excited across the bandgap at a low rate. However, the indirect bandgap also makes it harder for the excited electrons to drop back into the VB [7].

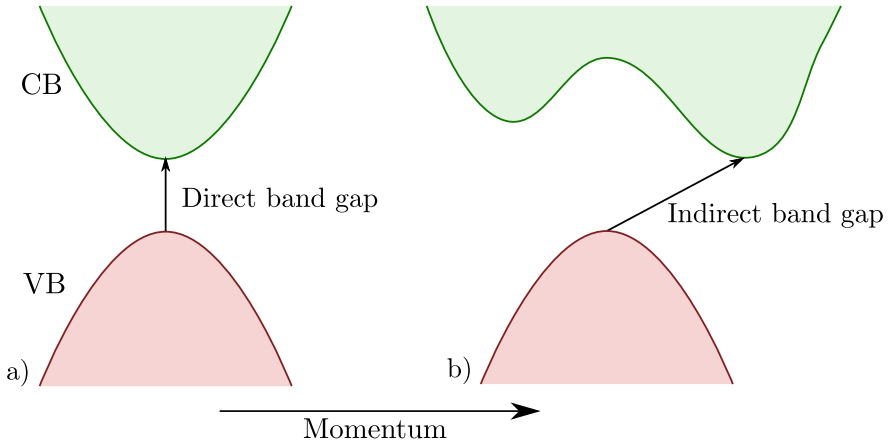

Figure 2.3: A material with a) direct bandgap, and b) indirect bandgap. Redrawn from [7].

Intrinsic semiconductors ideally have perfect crystal structures with no impurities. However, real materials do contain some impurities and dislocations. Impurity atoms can give rise to states inside the bandgap [7]. It is also possible to add impurities by introducing impurity atoms to an intrinsic semiconductor. This changes the conduction properties of the material significantly. Such a process is called *doping* [31]. The dopant atoms can either be donors or acceptors, as they either give (donate) electrons to the CB or take (accept) electrons from the VB by generating holes [30]. Since Si PV cells will be used in this master project, the doping of Si crystals will now be explained.

A Si atom is a group IV atom and thus has four outer electrons. In a Si crystal, four Si atoms share these electrons and form a full VB and an (indirect) bandgap of 1.1 eV to the CB. If a donor atom with five outer electrons (group V atom), such as phosphorus (P), is replaced with a Si atom in the Si crystal, four of its outer electrons will bond to four Si atoms, while the fifth electron will only be loosely bound to the dopant atom. Thus, it can easily be excited into the CB. The donor energy levels are located just below the minimum of the CB and the Fermi energy of the doped crystal moves closer to the CB, as illustrated in fig. 2.4 b). Si doped in this way is called n-type Si. Similarly, when an acceptor atom with three outer electrons (group III atom), such as boron (B), is replaced with a Si atom in the Si crystal, it does not have enough electrons to fully bond with its neighboring Si atoms. Thus, it can easily accept an electron from the top of the VB, resulting in a positive hole in the VB. The acceptor energy levels are located just above the maximum of the VB and now the Fermi energy moves closer to the VB, as illustrated in fig. 2.4 c). Si doped in this way is called p-type Si [7, 30, 31].

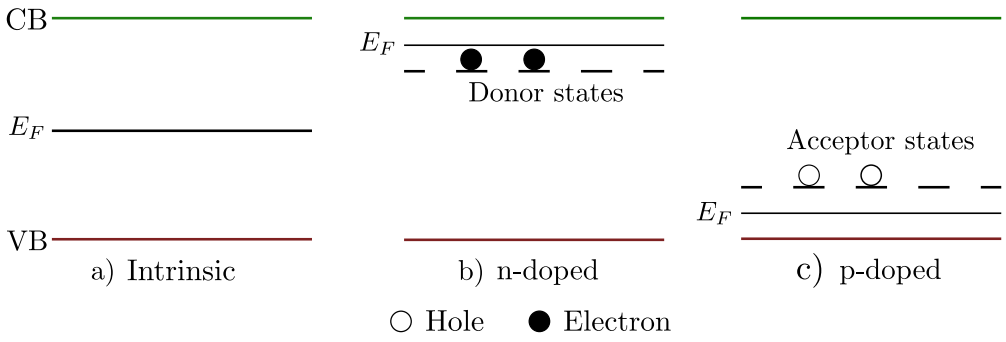

Figure 2.4: Illustration of the Fermi level in an a) intrinsic, b) n-doped and c) p-doped semiconductor. b) and c) also shows the donor and acceptor states, respectively [30].

When an n-type and a p-type semiconductor are joined, a p-n junction is formed. The process is illustrated in fig. 2.5. The loosely bound electrons on the n-side diffuse into the p-side, while the loosely bound holes on the p-side diffuse into the n-side. This results in a net flow of positive charge from the p-side to the n-side, known as the *diffusion current*, $I_{diffusion}$. The diffusing electrons and holes recombine when they meet, resulting in *depletion regions* on both sides of the interface, with immobile and ionized acceptors and donors, respectively. The depletion regions have opposite charge. The n-side is positive and the p-side is negative. An electric field across the junction is generated due

to the charged depletion regions, pointing from positive (n) to negative (p) side. This results in a potential difference V_0 between the two semiconductors, as illustrated in fig. 2.5 a). The electric field causes electrons to drift from the p-side to the n-side. This drift of electrons gives rise to the *drift current*, I_{drift}. Equilibrium is reached when the diffusion current and the drift current balance [7, 30]. The magnitude of the diffusion current and drift current in equilibrium is defined as I_0

$$|I_{diffusion}| = |I_{drift}| \equiv I_0 \tag{2.2}$$

As can be seen in fig. 2.5 b), the Fermi levels in the two materials align in equilibrium. Away from the depletion regions, the materials act as regular semiconductors that conduct current. However, in the depletion regions there are no mobile charge carriers and the materials act as insulators [7].

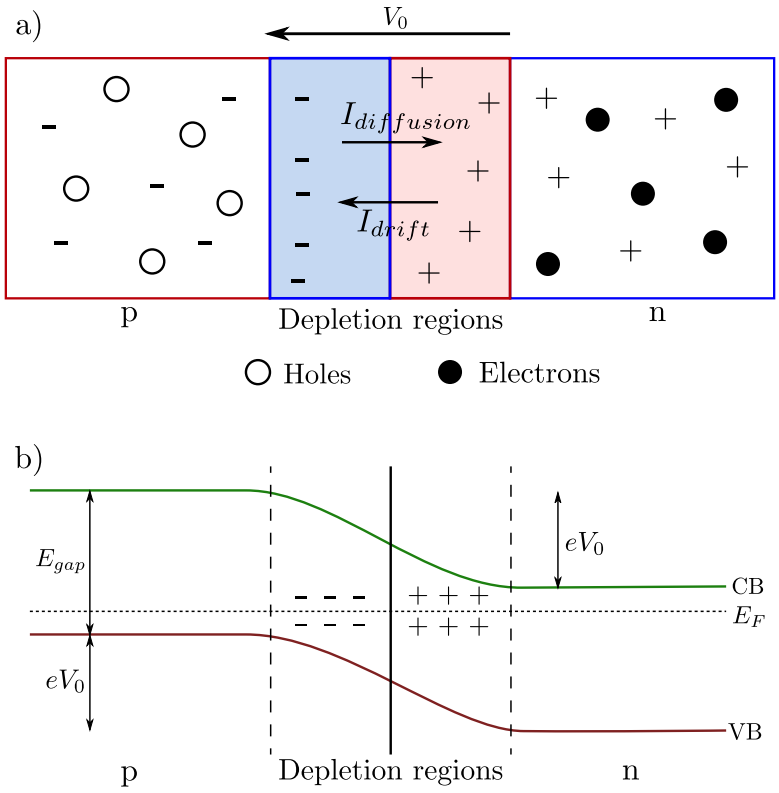

Figure 2.5: a) The p-n junction arising when a p- and n-doped semiconductor are joined. b) Band diagram of the p-n junction in equilibrium, illustrating the alignment of the two Fermi levels [30].

2.1.2 Working Principle

For a PV cell to function, there are some basic steps that must take place. First, the incoming solar radiation (photons) must be absorbed by the semiconductor and excite electrons from the VB to the CB, thereby generating electron-hole pairs. For the photons

to be absorbed, their energy must be greater than the bandgap of the semiconductor. The number of electron-hole pairs generated increases with the light intensity [29]. Secondly, the electron-hole pairs must be separated and driven through an external circuit. The separation is done by exploiting the inherent potential difference in the p-n junction, which drives the electrons to the n-side and the holes to the p-side. This generates an additional current I_{photo} in the same direction as I_0. In the presence of an external voltage V, the total current is [7]

$$I = I_{photo} - I_0(e^{eV/k_BT} - 1) \tag{2.3}$$

Electrons (holes) will now flow from the n-type (p-type) region to the p-type (n-type) region through the external circuit, given that the external voltage is not too large. Thus, there is a current flowing around the circuit in the direction of the photocurrent [7]. A cross section of a single junction (i.e. only one p-n junction) PV cell is depicted in fig. 2.6.

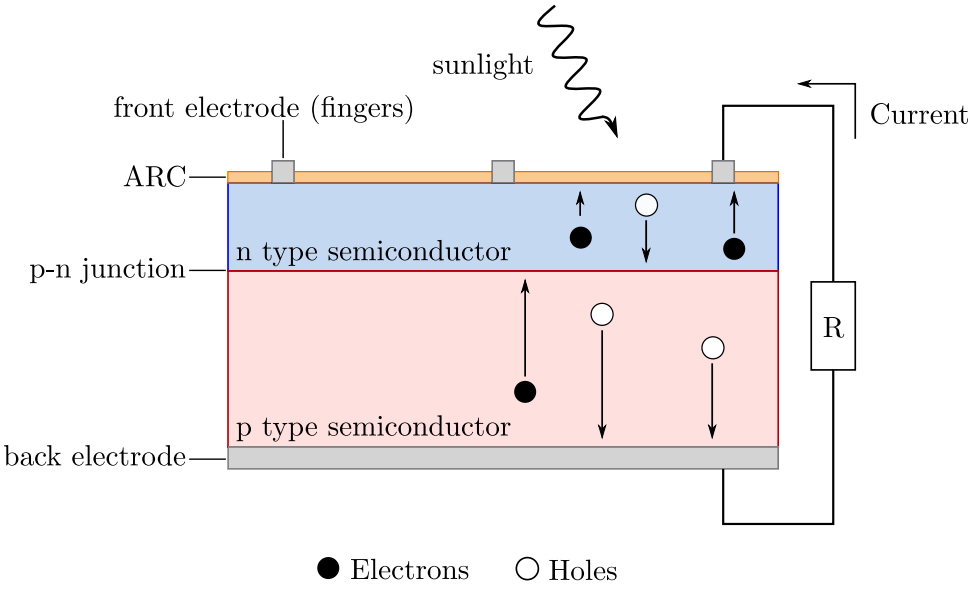

Figure 2.6: A cross section of a single junction PV cell, showing the p- and n-type material, the p-n junction, the ARC, the front and back electrodes and the external circuit. Redrawn from [32].

2.1.3 Characteristics of Photovoltaic Solar Cells

The current-voltage (IV) characteristics of an illuminated PV cell is presented in fig. 2.7. When the applied voltage is zero, the current is at its highest and is called the *short-circuit current*, I_{sc}. The short-circuit current equals the photogenerated current I_{photo}. The voltage has its maximum when the current is zero and is therefore known as the *open-circuit voltage*, V_{oc}. It reads as follows

$$V_{oc} = \frac{k_B T}{e} \ln\left(\frac{I_{sc}}{I_0} + 1\right) \tag{2.4}$$

There is an upper bound on V_{oc} due to electron-hole recombination. This results in a reduction of the power that can be extracted from a PV cell, given by the ratio eV_{oc}/E_{gap}. For practical Si devices with $V_{oc} \cong 0.7$ V, the ratio is approximately 0.64 [7].

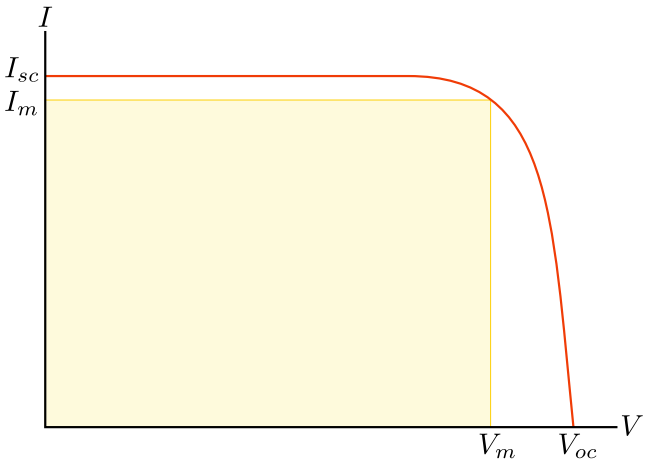

Figure 2.7: The IV characteristics of an illuminated PV cell. The yellow square is the product $I_m V_m$, that is, the maximum power that can be generated by the PV cell [7].

The total power output of a PV cell is given by the relation

$$P = IV \tag{2.5}$$

and is always less than the product $I_{sc}V_{oc}$. The voltage and current that gives the maximum total power output is V_m and I_m, respectively. The *fill factor*, ff, is defined as the ratio of the maximum total power output and the product $I_{sc}V_{oc}$ [29]:

$$\text{ff} = \frac{I_m V_m}{I_{sc} V_{oc}} \tag{2.6}$$

The lower the fill factor, the lower the efficiency of the PV cell. The fill factor of a typical Si PV cell ranges approximately from 0.85 - 0.87 [7].

As mentioned in the previous section, only the photons with energy greater than the bandgap E_{gap} can excite electrons from the VB to the CB in a PV cell. Therefore, photons with lower energy than E_{gap} are transmitted through the PV cell and do not contribute to the production of electrical energy. In addition, electrons excited by photons with energy greater than E_{gap} will thermalize in the CB, and the excess energy, the energy above E_{gap}, is lost. Thus, there is an upper bound on how much energy a PV cell can extract from the incoming radiation, denoted $\eta^{max}_{collection}$. The upper bound on collection efficiency for Si, with a bandgap $E_{gap} \cong 1.1$ eV, for AM1.5 radiation is $\eta^{max}_{collection} \leq 49$ % [7].

As is evident from the above discussion, there is an upper limit on the efficiency of a PV cell constructed from a semiconductor. This limit is known as the *Shockley-Queisser Limit*, and is the product of the fill factor ff, the maximum collection efficiency $\eta_{collection}^{max}$ and the ratio eV_{oc}/E_{gap} [7]:

$$\eta_{max} = \text{ff} \times \frac{eV_{oc}}{E_{gap}} \times \eta_{collection}^{max} \tag{2.7}$$

The theoretical η_{max} for a Si PV cell is approximately 33 % [7]. Real Si PV cells, however, have achieved efficiencies of about 25 % [30], while the best commercial PV cells have efficiencies of roughly 20 % (2017) [7]. The efficiency of PV cells is measured under standard conditions, which is an insolation of 1000 W/m^2, a cell temperature of 25 °C and AM1.5 solar spectrum [10].

2.2 Plasmonics

Plasmonics is the study of the fundamentals and applications related to *surface plasmons*. Surface plasmons are collective oscillations of the conduction electrons excited by electromagnetic waves at the interface between a conductor and a dielectric [33, 34]. There exist both surface plasmon polaritons and localized surface plasmons, and these will be further elucidated later, but first, the physics of the interaction between electromagnetic fields and matter is described.

2.2.1 The Dielectric Function

To describe the plasmon excitations in metal nanoparticles, a classical approach is sufficient [35]. In classical physics the interaction between matter and electromagnetic fields is described by Maxwell's equations as follows:

$$\nabla \cdot \mathbf{D} = \rho_{ext} \tag{2.8a}$$
$$\nabla \cdot \mathbf{B} = 0 \tag{2.8b}$$
$$\nabla \times \mathbf{E} = -\frac{\partial \mathbf{B}}{\partial t} \tag{2.8c}$$
$$\nabla \times \mathbf{H} = \mathbf{J}_{ext} + \frac{\partial \mathbf{D}}{\partial t} \tag{2.8d}$$

where $\mathbf{D}$ is the electric displacement, $\mathbf{B}$ is magnetic induction, $\mathbf{E}$ is the electric field, $\mathbf{H}$ is the magnetic field, ρ_{ext} and $\mathbf{J}_{ext}$ is external charge and current density, respectively [34]. In linear, homogeneous and isotropic materials these are related via

$$\mathbf{J} = \sigma \mathbf{E} \tag{2.9a}$$
$$\mathbf{D} = \varepsilon_0 \varepsilon \mathbf{E} \tag{2.9b}$$
$$\mathbf{B} = \mu_0 \mu \mathbf{H} \tag{2.9c}$$

Here, σ is the conductivity, ε_0 and μ_0 is the electric permittivity and the magnetic permeability of vacuum, respectively, μ is the relative permeability and ε is the dielectric constant. Eq. 2.9b indicates that $\mathbf{D}$ reacts instantaneously to $\mathbf{E}$. This is not the case for real material and therefore, the dielectric function is introduced. The dielectric function is a function of the wave vector $\mathbf{K}$ and the angular frequency ω:

$$\varepsilon(\mathbf{K}, \omega) = 1 + \frac{i\sigma(\mathbf{K}, \omega)}{\varepsilon_0 \omega} \tag{2.10}$$

This can be simplified for a spatially local response by letting $\mathbf{K} = 0$ such that the dielectric function is a function of ω only, $\varepsilon(\omega)$, for light-matter interactions. Thus, the dielectric function is given as

$$\varepsilon(\omega) = 1 + \frac{i\sigma(\omega)}{\varepsilon_0 \omega} \tag{2.11}$$

Both the dielectric function and the conductivity are complex-valued functions and can be written as

$$\varepsilon(\omega) = \varepsilon_1(\omega) + i\varepsilon_2(\omega) \tag{2.12a}$$

$$\sigma(\omega) = \sigma_1(\omega) + i\sigma_2(\omega) \tag{2.12b}$$

ε_1 and σ_2 describes the polarization of the material when exposed to an external electric field, which affects how electromagnetic waves propagate in the medium. The amount of absorption in the medium is determined by ε_2 and σ_1 [34]. The complex refractive index $\tilde{n}(\omega)$ is defined as the square root of the dielectric function:

$$\tilde{n}(\omega) = \sqrt{\varepsilon(\omega)} \tag{2.13}$$

A simple model to explain the electromagnetic response of metal subjected to an electromagnetic field is the Drude model, developed by the German physicist Paul Drude in 1900 [30]. In this model, the metal acts as plasma with a free electron gas and fixed positive ion cores, while electron-electron interactions and details of the lattice potential are ignored. Each electron has an effective optical mass m, which is assumed to include some aspects of the band structure. The plasma is excited by an external electromagnetic field, causing the electrons to start oscillating. Their oscillation is damped through collisions with a collision frequency $\gamma = 1/\tau$, where τ is the relaxation time of the free electron gas. At room temperature, τ is on the order of 10^{-14} s. If the driving electric field has a harmonic time dependence, $\mathbf{E}(t) = \mathbf{E}_0 e^{-i\omega t}$, the dielectric function is given as [34]

$$\varepsilon(\omega) = 1 - \frac{\omega_p^2}{\omega^2 + i\gamma\omega} \tag{2.14}$$

Here, ω_p is the plasma frequency of the free electron gas. It is defined as

$$\omega_p^2 = \frac{ne^2}{\varepsilon_0 m} \tag{2.15}$$

where n is the electron density, e is the electron charge and m is the effective optical mass of the electrons. For frequencies close to ω_p, damping is negligible and $\varepsilon(\omega)$ is mainly real. The simplified expression for the dielectric function is then [34]

$$\varepsilon(\omega) = 1 - \frac{\omega_p^2}{\omega^2} \tag{2.16}$$

$\varepsilon(\omega)$ is real and negative for $\omega < \omega_p$, thus resulting in a purely imaginary refractive index $\tilde{n} = \sqrt{\varepsilon}$. This means that the light impinging on the metal is reflected, due to conservation of energy. For $\omega > \omega_p$, $\varepsilon(\omega)$ is real and positive, resulting in a real refractive index. Hence, the light waves can propagate into the metal. Thus, the plasma frequency ω_p represents a transition of metals from being reflective to transparent. For most metals, the plasma frequency lies in the ultra-violet regime of the electromagnetic spectrum [30].

2.2.2 Surface Plasmon Polaritons

Surface plasmon polaritons (SPPs) are electromagnetic excitations that propagate on the surface between a conductor and a dielectric material [34]. The SPPs are evanescently confined in the direction perpendicular to the direction of propagation, meaning that the electromagnetic field of an SPP decays exponentially into the metal and the dielectric [35]. This is only possible if the real part of the dielectric function of the two media has opposite sign. In a metal, $\mathrm{Re}[\varepsilon(\omega)] < 0$, while a dielectric has a dielectric constant $\varepsilon_m > 0$. Thus, SPPs can only be excited on the surface of a metal and a dielectric. SPPs are described by a dispersion relation derived from Maxwell's equations with suitable boundary conditions [36]. The result is

$$\beta = k_0 \sqrt{\frac{\varepsilon(\omega)\varepsilon_m}{\varepsilon(\omega) + \varepsilon_m}} \tag{2.17}$$

The complex parameter β is the propagation constant. $k_0 = \omega/c = 2\pi/\lambda$ is the wave vector of the propagating wave in vacuum. The light line of the dielectric, $k = \sqrt{\varepsilon}(\omega/c)$, is always greater than the dispersion relation of the SPPs. To excite the SPPs, the momentum of the incident light ($\hbar k$) and the SPPs ($\hbar\beta$) has to be equal, which is never the case. Thus, the SPPs cannot be excited directly by light due to conservation of momentum. To excite SPPs, phase-matching techniques such as prism and grating coupling, must be employed [34].

2.2.3 Localized Surface Plasmons

In contrast to the propagating SPPs, excitation of the conduction electrons in metal nanoparticles form standing waves. These non-propagating waves form when a metal nanoparticle is coupled to an electromagnetic field. When the conduction electrons are excited, they are collectively displaced from the fixed ion-cores, and a restoring force is set up. This makes them oscillate collectively [35]. If the frequency of the incoming electromagnetic field is the same as the eigenfrequency of these oscillations, localized

surface plasmon resonance (LSPR) can occur. Among others, this leads to resonantly enhanced scattering and absorption [34].

The Quasi-Static Approximation

When the particle size d is much smaller than the wavelength of the incident light, $d << \lambda$, the electromagnetic field is approximately constant over the particle volume, and retardation effects can be ignored. This is called the *quasi-static approximation*. Then the interaction between the particle and the electromagnetic field can be described using electrostatics instead of electrodynamics [35].

The resonance condition can be described using a simple geometry illustrated in fig. 2.8, namely a homogeneous, isotropic sphere of radius a with a dielectric function ε. The sphere is located at the origin in a uniform, static electric field applied in the z-direction, $\mathbf{E} = E_0\hat{\mathbf{z}}$. The dielectric constant of the non-absorbing and isotropic surrounding medium is ε_m. The initially uniform electric field will be distorted due to the difference in permittivity. By first calculating the electrostatic potential given by the Laplace equation, $\nabla^2\Phi = 0$, the electric field can be calculated as follows [35]

$$\mathbf{E} = -\nabla\Phi \tag{2.18}$$

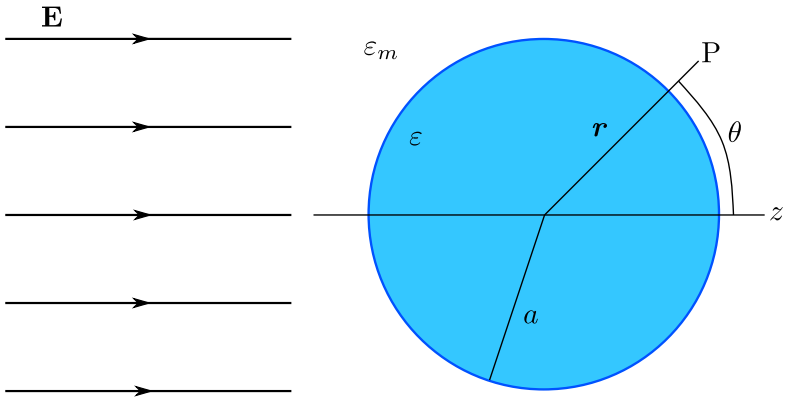

Figure 2.8: Metal sphere in a uniform static electric field. Redrawn from [37].

In terms of the Legendre-polynomials $P_l(\cos\theta)$, the general solution for the potentials inside and outside the metal sphere can be written as

$$\Phi_{in}(r,\theta) = \sum_{l=0}^{\infty}[A_l r^l]P_l(\cos\theta), \qquad r \leq a \tag{2.19a}$$

$$\Phi_{out}(r,\theta) = \sum_{l=0}^{\infty}[B_l r^l + C_l r^{-(l+1)}]P_l(\cos\theta), \qquad r \geq a \tag{2.19b}$$

where θ is the angle between the position vector $\boldsymbol{r}$ in the point P and the z-axis, as shown in fig. 2.8, and l is the order of the Legendre-polynomials. As can be seen from eqs. 2.19,

the potentials are independent of the azimuthal angle ϕ due to symmetry. To determine the coefficients A_l, B_l and C_l, boundary conditions at $r \to \infty$ and $r = a$ are used. As r approaches infinity, the electric field should behave as if the sphere was not there, that is, the potential outside the sphere should approach the initial potential. Mathematically, the following is required [37]

$$\lim_{r\to\infty} \Phi_{out} = -E_0 z = -E_0 r\cos(\theta) \tag{2.20}$$

At the sphere surface $r = a$, the tangential components of the electric field and the normal components of the displacement field must be continuous, giving the following boundary conditions

$$-\frac{1}{a}\frac{\partial \Phi_{in}}{\partial \theta}|_{r=a} = -\frac{1}{a}\frac{\partial \Phi_{out}}{\partial \theta}|_{r=a} \tag{2.21a}$$

$$-\varepsilon_0\varepsilon\frac{\partial \Phi_{in}}{\partial \theta}|_{r=a} = -\varepsilon_0\varepsilon_m\frac{\partial \Phi_{out}}{\partial \theta}|_{r=a} \tag{2.21b}$$

Solving eqs. 2.19 by applying the boundary conditions given by eqs. 2.20 and 2.21, the potentials evaluate to

$$\Phi_{in}(r,\theta) = -\frac{3\varepsilon_m}{\varepsilon + 2\varepsilon_m}E_0 r\cos\theta \tag{2.22a}$$

$$\Phi_{out}(r,\theta) = -E_0 r\cos\theta + \frac{\varepsilon - \varepsilon_m}{\varepsilon + 2\varepsilon_m}E_0 a^3\frac{\cos\theta}{r^2} = -E_0 r\cos\theta + \frac{\mathbf{p}\cdot\mathbf{r}}{4\pi\varepsilon_0\varepsilon_m r^3} \tag{2.22b}$$

E_0 is the amplitude of the applied field and $\mathbf{p}$ is the dipole moment, defined as

$$\mathbf{p} = 4\pi\varepsilon_0\varepsilon_m a^3\frac{\varepsilon - \varepsilon_m}{\varepsilon + 2\varepsilon_m}\mathbf{E}_0 \tag{2.23}$$

Eq. 2.22b is the superposition of the field of an ideal dipole located at the particle center, with dipole moment $\mathbf{p}$, and the applied field [37]. Thus, a dipole moment is induced in the sphere by the applied field. The dipole moment can be described by the polarizability α by the relation $\mathbf{p} = \varepsilon_0\varepsilon_m\alpha\mathbf{E}_0$. The polarizability describes how easily the sphere is polarized by the electric field, and for a sub-wavelength sphere it is given as

$$\alpha = 4\pi a^3\frac{\varepsilon - \varepsilon_m}{\varepsilon + 2\varepsilon_m} \tag{2.24}$$

Eq. 2.24 clearly shows that a resonant enhancement is experienced by the polarizability when $|\varepsilon + 2\varepsilon_m|$ is a minimum. For slowly-varying or small $\mathrm{Im}[\varepsilon]$ around the minimum, the resonance condition is given by the Fröhlich condition [34]

$$\mathrm{Re}[\varepsilon(\omega)] = -2\varepsilon_m \tag{2.25}$$

The Fröhlich condition states that the resonance frequency depends strongly on the dielectric medium surrounding the sphere. As ε_m increases, the resonance red-shifts [34].

By changing the surrounding medium it is possible to tune the spectral position of the LSPR.

Together, eqs. 2.18 and 2.22 give the electric fields:

$$\mathbf{E_{in}} = \frac{3\varepsilon_m}{\varepsilon + 2\varepsilon_m}\mathbf{E}_0 \tag{2.26a}$$

$$\mathbf{E_{out}} = \mathbf{E}_0 + \frac{3\mathbf{n}(\mathbf{n}\cdot\mathbf{p}) - \mathbf{p}}{4\pi\varepsilon_0\varepsilon_m}\frac{1}{r^3} \tag{2.26b}$$

Here, $\mathbf{n}$ is the unit vector in the direction from the center of the sphere to the point P. From eqs. 2.26, it is clear that the electric fields both inside and outside the metal sphere experience a resonant enhancement when the Fröhlich condition is fulfilled. In section 2.2.2, it is stated that the electromagnetic fields decay exponentially into metals. However, eq. 2.26 states that the electric field is homogeneous inside the metal sphere. Hence, the quasi-static approximation is only valid when the diameter of the metal sphere is larger than the skin depth of the metal.

In the quasi-static approximation, the metal sphere is described as a dipole which both scatters and absorbs light. When the polarizability α is resonantly enhanced, the scattering and absorption efficiency of the metal sphere is enhanced as well. The probability of a particle to scatter or absorb light is termed the cross section, denoted C_{sca} and C_{abs}, respectively. The cross sections are given as

$$C_{sca} = \frac{k^4}{6\pi}|\alpha|^2 = \frac{8\pi}{3}k^3a^6|\frac{\varepsilon - \varepsilon_m}{\varepsilon + 2\varepsilon_m}|^2 \tag{2.27a}$$

$$C_{abs} = k\ \mathrm{Im}[\alpha] = 4\pi k a^3 \mathrm{Im}[\frac{\varepsilon - \varepsilon_m}{\varepsilon + 2\varepsilon_m}] \tag{2.27b}$$

$k = 2\pi/\lambda$ is the wavenumber. Clearly, both the scattering and absorption cross sections experience a resonant enhancement when the Fröhlich condition is fulfilled. For large particles, the scattering efficiency is dominant, as C_{sca} scales with a^6, while the smaller the particle gets, the more significant is the absorption efficiency, as C_{abs} scales with a^3. The sum of the absorption and scattering is defined as extinction. For a sphere with dielectric function $\varepsilon(\omega) = \varepsilon_1(\omega) + i\varepsilon_2(\omega)$, the extinction cross section is given as [34]

$$C_{ext} = C_{abs} + C_{sca} = 9\frac{\omega}{c}\varepsilon_m^{3/2}V\frac{\varepsilon_2}{[\varepsilon_1 + 2\varepsilon_m]^2 + \varepsilon_2^2} \tag{2.28}$$

Eq. 2.24 describes the polarizability of metal spheres. However, other simple geometries, such as spheroids, can also be explained in the quasi-static approximation. For a spheroid, the polarizability is given in terms of a geometric factor. Due to oscillations of its conducting electrons along both the minor and major axis, the spheroid exhibits two spectrally separated resonances. Thus, the spectral position of the LSPR can be tuned either by changing the surrounding medium or by changing the aspect ratio of the metal nanoparticle [34].

Mie Theory

In the quasi-static approximation, it is assumed that the electric field is constant over the whole particle volume, and phase-changes of the field is not taken into account. This is a good approximation as long as the particle size is much smaller than the wavelength of the incident light. However, for particles as small as 10 % of the wavelength it is necessary with an electrodynamic approach [35]. In 1908, the German physicist Gustav Mie developed a complete theory of the scattering and absorption of electromagnetic radiation by a sphere of arbitrary radius and refractive index [37]. In this theory, higher order resonances are taken into account. The electromagnetic radiation incident on a metal nanoparticle will excite higher order modes and not just the dipolar mode described by the quasi-static approximation. The dipolar mode is retained when only the first order resonance is considered. For larger particles, however, higher order terms have to be considered as well [34].

2.2.4 Factors Affecting the Localized Surface Plasmon Resonance

The resonant properties of metal nanoparticles are affected by many factors. This makes it possible to tune the spectral position, width and height of the resonance peak or peaks.

Shape of Particle

The spectral position of the LSPR peak and the number of peaks is highly dependent on the shape of the nanoparticle. Because of its high symmetry, an isolated metal sphere exhibits a single LSPR peak, which can be shifted by changing the size of the particle, as will be described in the next paragraph. However, asymmetric particles may exhibit several LSPRs. In spheroidal metal nanoparticles, the oscillations of the conduction electrons along the major and minor axis give rise to two spectrally separated LSPRs. Within the quasi-static approximation, when the aspect ratio increases compared to a sphere of the same volume the resonance due to oscillations along the major axis are red-shifted. An ellipsoidal metal nanoparticle may exhibit three separate resonances. For certain asymmetries, such as nanowires, higher order resonances may be observed [34].

Size of Particle

As described in section 2.2.3, the quasi-static approximation is only valid when the particle size is much smaller than the wavelength of the incident light. In the quasi-static approximation, two regimes are not described. Firstly, when the particle size exceeds the quasi-static limit, an electrodynamic approach is required due to retardation effects across the particle volume [35]. Particles of this size are described by Mie theory, which states that the retardation effects lead to a shift in the plasmon resonance. As the particle size increases, the spectral position of the (dipolar) resonance redshifts. In addition, Mie theory predicts the occurrence of higher order resonances and a broadening of the

linewidth of the LSPR peak as the particle diameter increases due to radiation damping [34]. Secondly, the regime where the mean free path of the particle's oscillating electrons is longer than the particle dimensions. As the particle size decreases, electron-surface scattering leads to LSPR broadening [38].

Particle Ensembles

The interactions between neighboring particles in an ensemble can change the LSPR wavelength compared to that of a single particle of the same material. Depending on the distance between the particles, near-field or far-field interactions affect the spectral position of the LSPR.

For closely spaced particles of size a and with interparticle distance d, where $a << d$ and $d << \lambda$, near-field interactions are dominating with a distance dependence of d^{-3} [34]. If the incident electric field is polarized parallel to the long particle pair axis, the restoring force between the oscillating electrons of each particle is weakened, resulting in a red-shift of the LSPR. In contrast, the restoring force is increased when the incident electric field is polarized normal to the long particle pair axis, and thus results in a blue-shift of the LSPR, [39]. Both of these scenarios are illustrated in fig. 2.9. Near-field coupling may also affect single particles of a complex structure [34].

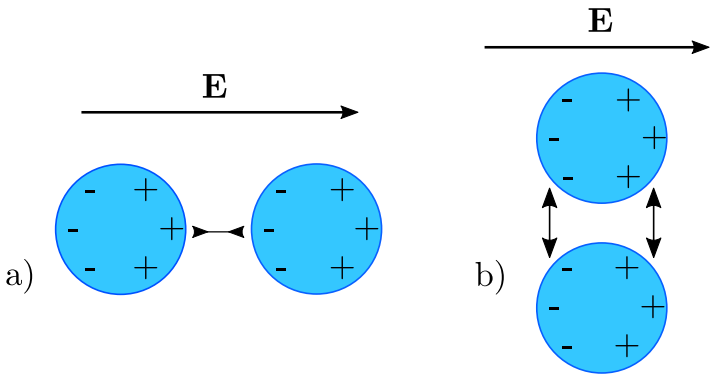

Figure 2.9: Near-field interactions between metal nanoparticles when the electric field is polarized a) parallel to the long particle pair axis and b) normal to the long particle pair axis [39].

For particle separations exceeding those allowing near-field coupling, far-field coupling via diffraction dominates, with a distance dependence of d^{-1} [34]. These interactions are due to the scattered light fields of the nanoparticles, and relies on the periodicity of the array, and thus the grating constant. Lamprecht *et. al* [40] investigated square 2D arrays of circular gold (Au) nanoparticles of diameter 150 nm and height 14 nm with grating constants d varying from 350 to 850 nm. They found that the bandwidths (FWHM) of the extinction spectra were strongly different for the various grating constants d. In addition, they found no significant broadening or shift of the plasmon resonance for random particle distance distributions, which confirms that the far-field effects are determined by the periodicity of the square array.

Surrounding Medium

As mentioned in section 2.2.3, the resonance frequency is highly dependent on the dielectric medium surrounding the metal sphere. This is clearly stated in the Fröhlich condition given by eq. 2.25.

Structure of Particle

The structure of the nanoparticle also affects the LSPR. When a homogeneous sphere is coated with a shell of a different material, the LSPR shifts. How large the shift is depends on the dielectric function of the core as well as the coating material and its thickness [41].

2.3 Lumerical

In this thesis work, the simulation software Lumerical has been used. Lumerical is a software founded in 2003, offering different tools for photonic simulations. The package used in this thesis work is Lumerical's Finite Difference Time Domain (FDTD) solver. In complex geometries, the FDTD method is a good way for solving Maxwell's equations. Through Fourier transforms, FDTD obtains the frequency solution in addition to time and space solutions, and can therefore calculate transmission, reflection, the complex Poynting vector and other quantities [42].

Maxwell's curl equations in non-magnetic materials are solved in the FDTD solver, given by eqs. 2.8d, 2.9b and by inserting eq. 2.9c into eq. 2.8c. The latter gives

$$\nabla \times \mathbf{E} = -\frac{\partial \mathbf{B}}{\partial t} = -\frac{\partial \mu_0 \mathbf{H}}{\partial t} \Rightarrow \frac{\partial \mathbf{H}}{\partial t} = -\frac{1}{\mu_0} \nabla \times \mathbf{E} \tag{2.29}$$

Maxwell's curl equations are then (with $\mathbf{J}_{ext} = 0$)

$$\frac{\partial \mathbf{D}}{\partial t} = \nabla \times \mathbf{H} \tag{2.30a}$$

$$\mathbf{D}(\omega) = \varepsilon_0 \varepsilon_r(\omega) \mathbf{E}(\omega) \tag{2.30b}$$

$$\frac{\partial \mathbf{H}}{\partial t} = -\frac{1}{\mu_0} \nabla \times \mathbf{E} \tag{2.30c}$$

There are six electromagnetic field components in three dimensions: E_x, E_y, E_z, H_x, H_y and H_z. Each of these field components is solved on a discrete spatial and temporal grid cell, termed the *Yee cell*, illustrated in fig. 2.10. As is clear from the figure, the components are solved at slightly different locations within the cell, and then the results are interpolated to the origin of each grid point. The mesh that is used is a rectangular Cartesian mesh which is automatically generated by the solver. The simulations are more accurate for a smaller mesh. Therefore, a smaller mesh is generated in high index and highly absorbing materials to maintain a constant number of mesh points per wavelength. In addition, when having complex structures or rapidly changing fields it is possible to set the mesh size manually.

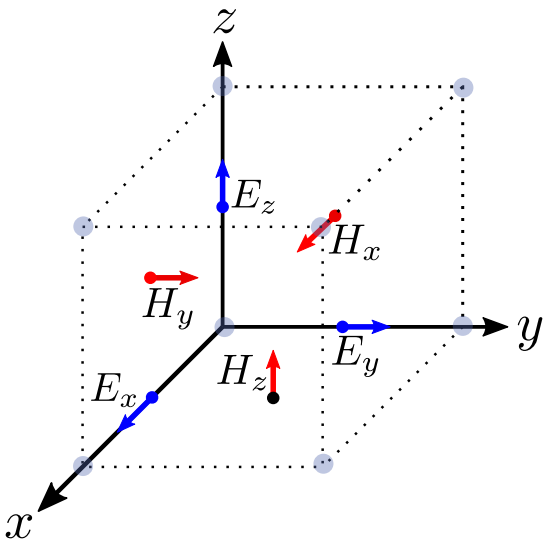

Figure 2.10: The Yee cell used for meshing. Redrawn from [42].

The FDTD solver offers a variety of sources, such as point dipoles, total-field scattered-field (TFSF) and plane waves. Parameters for many materials from which to build structures are also included in the software. Different boundary conditions (BCs) to the simulation region are also offered. This includes perfectly matched layer (PML), symmetric/anti-symmetric, periodic and Bloch BCs.

When illuminating a structure at an angle using a broadband plane wave source, Broadband Fixed Angle Source Technique (BFAST) must be used. Otherwise, the injection angle changes with frequency. In BFAST, the FDTD algorithm is reformulated so that the angle dependence is removed [43]. BFAST has its own built-in BCs transverse to the propagation direction. In the longitudinal direction, PML BCs should be used. When BFAST is used, some stability problems arise. However, these can be overcome by modifying the "dt multiplier" and the "bfast dt stability factor" found in the "Edit" window of the FDTD simulation region. In addition, the PML profile can be set to stabilized, which increases the number of PML layers. These modifications increase the simulation time, but are necessary to maintain stability. The greater the injection angle, the longer the simulation time [44].

The data is recorded using monitors. There are several monitors with different outputs, such as refractive index, movie monitors and frequency-domain field profile/power monitors.

Chapter 3

Methods

This chapter gives an overview of the methods used in this master thesis. First, a description of the simulation setup used is given, followed by an explanation of the different experimental setups used, and finally, the experimental equipment planned to use at Rice University is described.

3.1 Description of the Simulation Setup

Lumerical was used to measure the amount of incident power that entered a monocrystalline silicon (Si) PV cell coated with silicon nitride (Si_3N_4) as an ARC. A screenshot of the setup is shown in fig. 3.1. When the desired structure was created, an FDTD simulation region was defined. Inside this, the plane wave source and monitor were placed. For the results to be correct, it was important that the source injection plane and monitor extended outside the simulation region. The monitor used in this thesis was a frequency-domain field power monitor. The field profile in the frequency domain was collected from the simulation results by this monitor. From this, the electric and magnetic field through the monitor, as well as the Poynting vector, as a function of position and wavelength/frequency was calculated. In addition, the power transmitted through the monitor as a function of wavelength/frequency was calculated. The transmission results were normalized to the source power [42].

A monocrystalline Si slab of size 2.6 μm $\times$ 2.6 μm $\times$ 2 μm with an ARC coating of size 2.6 μm $\times$ 2.6 μm $\times$ 0.080 μm was used. A 2D frequency-domain field power monitor was placed 20 nm inside the Si slab to measure the amount of incident light that entered the Si slab. The monitor collected 40 data points per simulation. Different nanoparticles were placed on top of the ARC. A 3D FDTD simulation region was used. The plane wave source was located 1 μm above the top of the ARC. Its wavelength interval was from 300 to 900 nm as the amount of diffuse light outside this interval is negligible. The light source in FDTD is polarized, and both p- and s-polarizations were used.

In z-direction, PML BCs were used. When illuminating at an incident angle of 0°, periodic BCs were used. When illuminating at an angle $> 0°$, BFAST was used. This caused an increase in simulation time, but was necessary due to the broadband plane

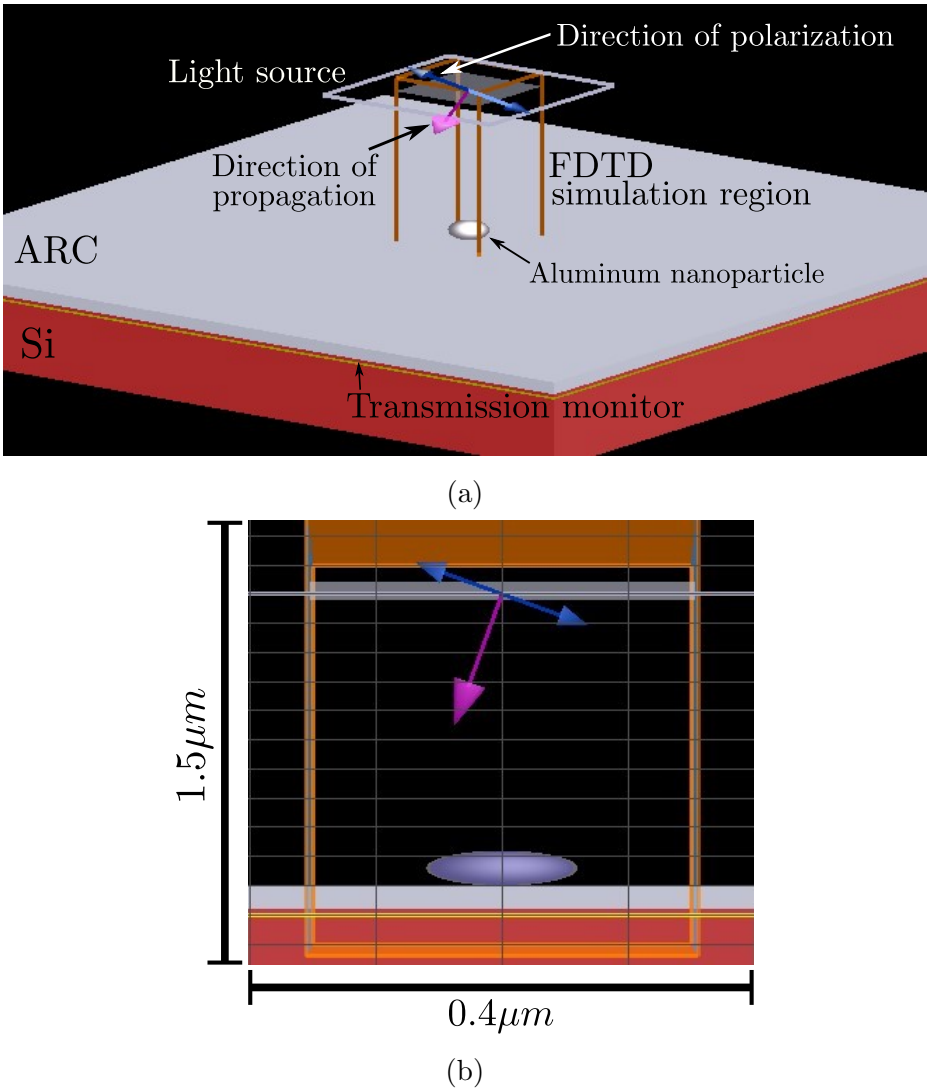

Figure 3.1: a) A perspective view of the simulation setup with an aluminum (Al) nanoparticle with a 3 nm thick oxide layer. The Al nanoparticle is placed in the middle of the Si slab (red) with the ARC layer (gray) on top. Above this, the plane wave source is placed. The pink arrow shows the direction of propagation, while the blue arrow shows the polarization of the E-field. The orange box is the FDTD simulation region. b) The same simulation setup in an xz-view. The yellow line inside the Si slab is the monitor used to measure the transmission.

wave source, as explained in section 2.3. When BFAST was used, the boundaries in x and y direction were periodic in accordance with the structure. Therefore, the dimension of the FDTD simulation region in x and y determined the period of the nanoparticles, that is, the distance between them.

Lumerical was also used to calculate the scattering and absorption cross sections for various nanoparticles when located on top of an ARC coated Si slab. To do so, a 3D TFSF

source was used to encapsulate the nanoparticle. The source ranged from 300 to 900 nm in wavelength. The TFSF source separates the computation region into one region that includes only the scattered field and one region that includes both the incident field and the scattered field. Two transmission boxes, which is an analysis group compromising six transmission monitors, were used to measure the absorption and scattering cross section. One was placed inside the TFSF source box, measuring the absorption, while the other was placed outside, measuring the scattering. PML BCs were used in order to prevent light to scatter back from the boundaries. The setup is depicted in fig. 3.2.

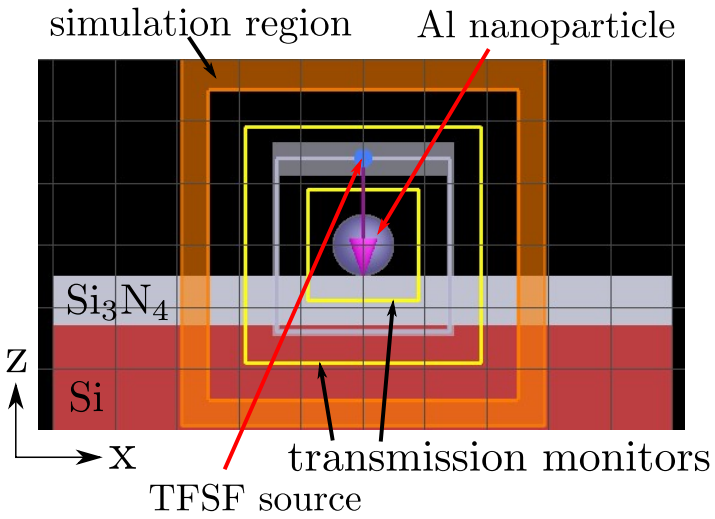

Figure 3.2: An xz-view of the simulation setup for the cross section calculations. The TFSF source is the gray box. The total field region is inside the box while the scattered field region is outside the box.

3.2 Experimental Setup

3.2.1 Characterizing the Photovoltaic Solar Cells

The PV cells used in this master thesis were standard monocrystalline Si PV cells with dimensions 2×2 mm. The PV cells were structured and coated with an 80 nm thick ARC, and were supplied by collaborators at the Institute for Energy Technology (IFE). An illustration of a PV cell is shown in fig. 3.3. At IFE, the PV cells were cut to the desired size using a laser. This process might change the performance or even damage the cells and it was important to test them after the laser cutting.

Two thin glass slabs were joined with tape so that there was a gap of about 1 mm between them. The PV cells were then fastened with carbon tape over the gap so that both the front and back electrodes could be contacted. Then, the glass plates were fastened to a holder in front of the light source. The light source used to illuminate the PV cells was an OSL1-EC high-intensity fiber light source from ThorLabs, with a lamp

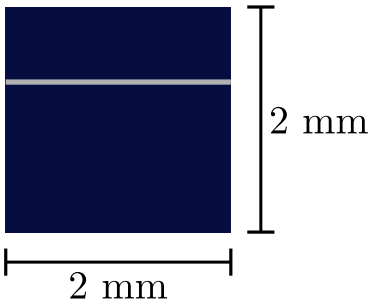

Figure 3.3: An illustration of the PV cells used. The gray line is the front electrode, termed "finger".

of 150 W [45]. Which light source to use was not important, as the aim only was to check that the PV cells worked. To focus the light onto the PV cell, a focusing lens was placed between the light source and the PV cell. This made the intensity of the light on the cell higher and more current was generated, making it easier to see the characteristic IV curve. Two micro-manipulators with needles on the tip were then used to contact the electrodes on the PV cell. The micro-manipulators were coupled to a potentiostat, which in turn was connected to a PC. The PC used the EC-Lab software from BioLogic to make IV characteristics of the PV cells. Fig. 3.4 shows a schematic of the experimental setup for characterizing the PV cells, while fig. 3.5 shows a photo of the same setup. The voltage interval was set to be from -1 to 1 V.

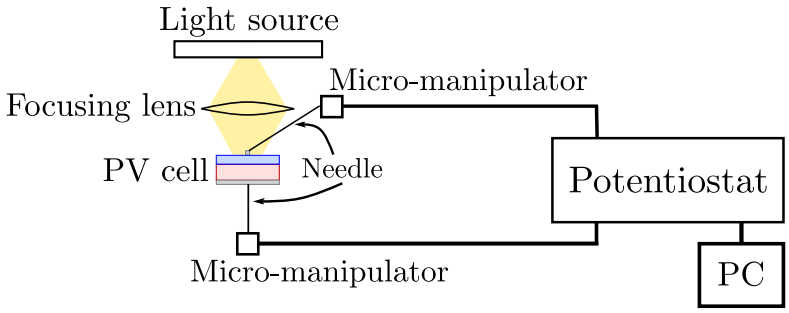

Figure 3.4: A schematic diagram of the experimental setup for characterizing the PV cells. The front- and back electrode of the PV cell was connected to the potentiostat through the needles on the micro-manipulators. The light was focused onto the PV cell through a focusing lens. Not to scale.

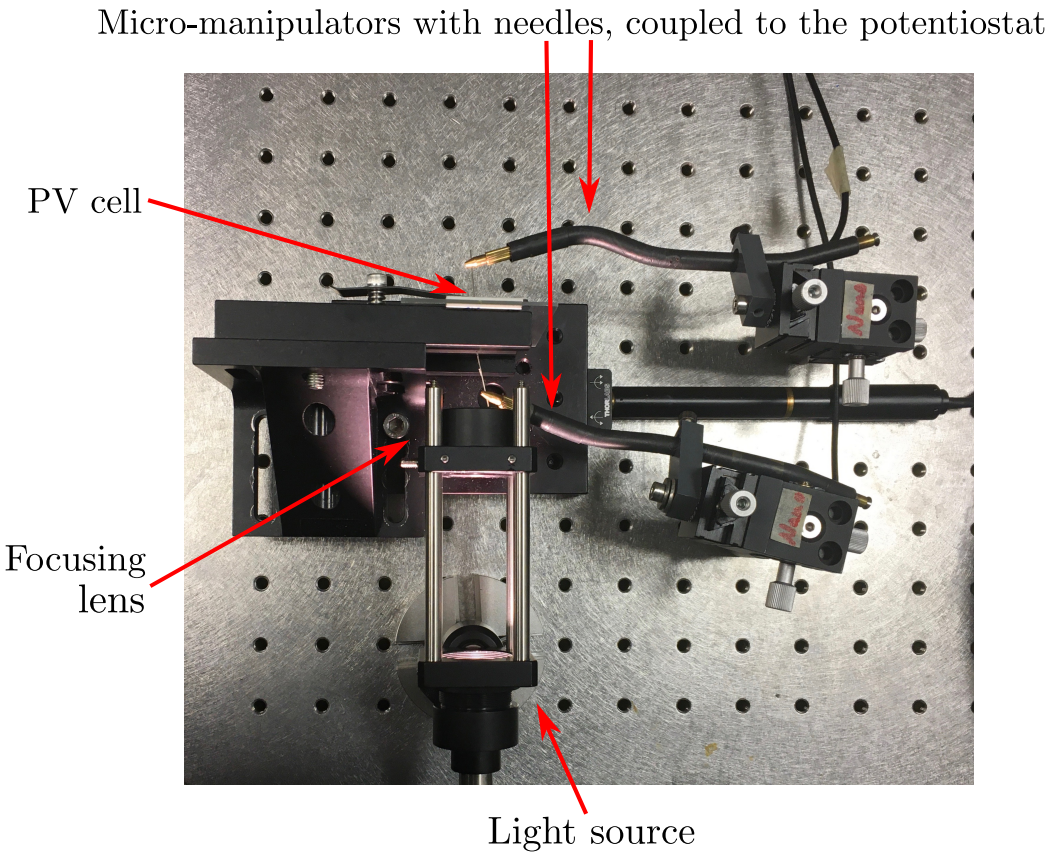

Figure 3.5: An photo of the experimental setup used when characterizing the PV cells. The micro-manipulators has a needle on the tip which was used to contact the electrodes on the PV cell. A focusing lens was used to focus the light onto the PV cell. The PV cell was fastened with carbon tape to a glass plate with a small gap in the middle, which made it possible to contact the PV cell on both sides.

3.3 Experiments Planned to be Performed at Rice University

As already mentioned, the stay at Rice University had to be terminated four weeks earlier than planned due to the outbreak of the COVID-19 pandemic. Therefore, there was not enough time to complete the experiments that were planned to do there. However, in the four weeks spent at Rice University I got training on all the relevant instruments and so a description of these instruments is included here for future reference. In section 5.2 a brief description of the experiments that were to be carried out is presented.

3.3.1 Preparation of Substrate

Since Si is not transparent, transmission measurements with an experimental setup equal to the simulation setup, consisting of Al nanoparticles on top of a flat Si slab coated with SiN_x, was not possible. Therefore, alternative transmission measurements had to be performed. Silicon oxide (SiO_2) is transparent, and it was therefore decided to make samples of SiO_2 coated with SiN_x. Thus, the transmission through the SiN_x layer could be measured.

The refractive index of SiO_2 is, in contrast to the refractive index of Si, smaller than the refractive index of SiN_x in the wavelength region 300 to 900 nm. Thus, light that is reflected off of the interface between SiO_2 and SiN_x is not out of phase with the light incident on the interface. Therefore, for the SiN_x layer to function as an ARC when coated on SiO_2 instead of Si, the thickness needs to be half of the wavelength in the coating, and not a quarter of the wavelength (see section 1.4.2). It was therefore decided to make the thickness of the SiN_x 160 nm.

Sputtering

To add a SiN_x coating on a SiO_2 sample, it was planned to use the AJA ATC Orion Sputter System for physical vapor deposition at the cleanroom of the Shared Equipment Authority (SEA) at Rice University, depicted in fig. 3.6. The system enables sputtering of metals, dielectrics and magnetic materials on substrate sizes up to 100 mm.

Sputtering is a vacuum coating process where a target is bombarded with energetic ions of an inert gas such that atoms or molecules are ejected from the target. The ejected material can then be coated directly onto substrates. For this to happen, high energy ions must be created and directed towards the target. The sputtering system at SEA at Rice University is a magnetron sputtering system, in which magnetic fields are used to ionize the gas and create the energetic ions. After the bombardment of the target, the atoms ejected are deposited on the substrate forming a thin film coating. To prevent collisions between the ejected atoms and the gas and to maintain high ion-energies, low pressure is required, which is why vacuum is necessary [47].

To deposit a SiN_x thin film on SiO_2, a Si_3N_4 target should be used. However, such a target was not in stock at SEA and had to be ordered. In the meantime, reactive

Figure 3.6: The AJA ATC Orion Sputter System at Rice University. Photo taken from [46].

sputtering tests using a Si target was carried out. In reactive sputtering, a reactive gas is added to the inert gas, in this case nitrogen (N) gas. The reactive gas reacts with the atoms ejected from the target and forms the desired thin film on the substrate [48]. A SiN_x thin film was deposited on a SiO_2 and a Si sample simultaneously, both approximately 1×1 cm^2. The latter was to be used in the ellipsometer to determine the thickness of the film, as will be described in the next section. The deposition was done with help of researchers at Rice University.

Ellipsometer

To check the thickness of the deposited SiN_x thin film, the J.A. Woollam M-2000DI ellipsometer at SEA at Rice University was planned to be used, depicted in fig. 3.7. An ellipsometer is used to accurately determine the real and imaginary part of the refractive index, thickness and absorption coefficient of a thin film [49]. In an ellipsometer, light from the light source passes through a polarizer before it irradiates the sample. The light is then reflected through an analyzer before it reaches the detector. By analyzing the change in polarization of the light reflected off of the sample, characteristics of the sample can be determined. The incident light angle can be varied [50]. A schematic diagram of an ellipsometer is presented in fig. 3.8.

Figure 3.7: The J.A. Woollam M-2000DI ellipsometer at Rice University. Photo taken from [46].

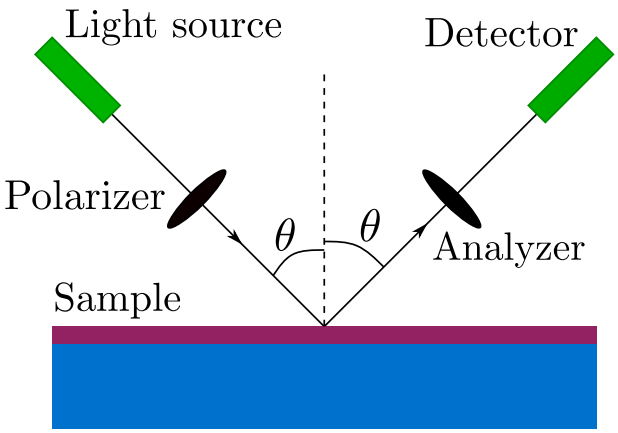

Figure 3.8: A schematic diagram of an ellipsometer.

3.3.2 Transmission Measurements

The Al nanoparticles were to be deposited on the substrates prepared with sputtering with the help of researchers at Rice University. The Al nanoparticles were synthesized chemically at Rice University, where nanoparticles with diameters ranging from 70 to 220 nm can be synthesized. The nanoparticles have a 2-4 nm oxide layer [51].

The angle-dependent transmission measurements were supposed to be done using a Zeiss Axiovert 200 MAT microscope connected to a computer, depicted in fig. 3.9. By using condensers of various numerical aperture (NA) and a dark-field insert into the beam path, only the edge of the light cone would illuminate the sample, giving angle-dependent transmission measurements.

Figure 3.9: The Zeiss Axiovert 200 MAT microscope at Rice University.

3.3.3 Dark-Field Microscopy

A custom-built UV-visible dark-field microscope was used to obtain the scattering spectra from both a bare etched PV cell sample from IFE and from single Al nanoparticles on top of a flat Si_3N_4 coated Si wafer. The coating was 83 nm thick, and the light was unpolarized. These measurements were done by a researcher at Rice University after the stay there was terminated. A schematic diagram of the dark-field microscope is illustrated in fig. 3.10.

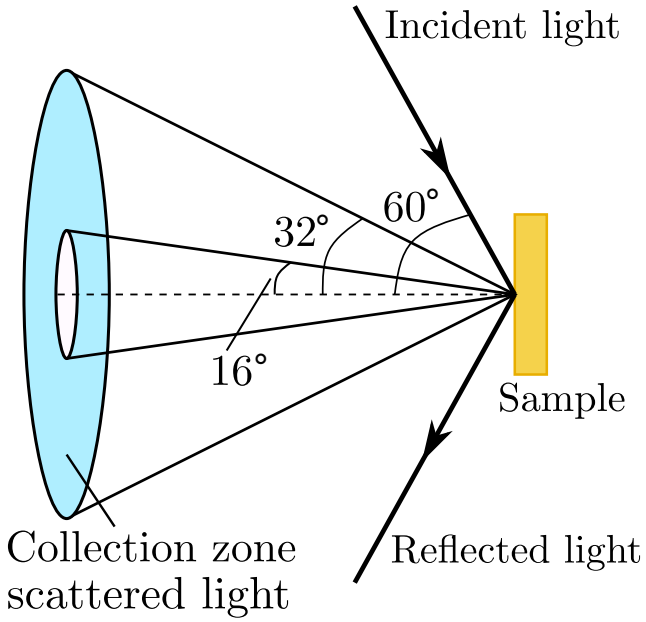

Figure 3.10: A schematic diagram of the dark-field microscope at Rice University.

Chapter 4

Results and Discussion - Simulations

This chapter presents the simulation results followed by a calculation of the overall efficiency increase of the PV cell. The addition of spherical aluminum nanoparticles with diameters ranging from 100 to 140 nm and with a 3 nm oxide layer on top of an ARC coated silicon slab gave the most promising results. In the wavelength range 400 to 900 nm the amount of light transmitted into the silicon slab increased by 7.46 % when these nanoparticles were added. The overall efficiency of a silicon PV cell with 120 nm in diameter aluminum nanoparticles on top increased by 1.71 %.

4.1 Selecting a Parameter Space for Simulations

In this section, it is argued how the parameter space was selected. An overview of the parameters is given in table 4.1 in the end of this section.

4.1.1 Substrate

Flat surfaces were used rather than the textured surfaces normally used for PV cells (see section 1.4.1). This was a deliberate choice to enhance the understanding of the physics of the systems investigated and to form a more simple setup for initial experiments. The simulations can easily be modified to be carried out for textured surfaces. In addition, since the nanoparticle size is an order of magnitude smaller than the height of the pyramids on the textured surfaces, relatively the substrate is flat. The substrate in all simulations was a silicon (Si) slab coated with an 80 nm thick silicon nitride (Si_3N_4) layer on top as an ARC, and various nanoparticles were then added on top of the ARC. The thickness of the ARC layer was chosen because the ARC layer on the PV cells from IFE, later to be used in experiments, was 80 nm thick. The refractive index of Si_3N_4 is close to two in the relevant wavelength range. Thus, a thickness of 80 nm corresponds to a maximum suppression of reflection at a wavelength of approximately 640 nm, where the intensity of the solar spectrum is high, see section 1.4.2 for further details.

4.1.2 Wavelength Range

The wavelength range was chosen based on the diffuse light spectra, shown in fig. 1.2. At wavelengths shorter than 300 nm there is very little diffuse light and this was set as the lower limit. When the wavelength exceeds 900 nm, the intensity of diffuse light again becomes small, and this was set as the upper limit. Thus, the wavelength interval was set to be 300 to 900 nm. As described in section 2.1.2, photons are only absorbed if their energy exceeds the bandgap of the semiconductor. The bandgap of Si is approximately 1.1 eV, corresponding to a wavelength of approximately 1130 nm. Thus, the wavelength interval 300 to 900 nm, where the intensity of diffuse light is of importance, is sufficient for the photons to be absorbed by Si.

As mentioned in chapter 3, the light source in Lumerical is polarized. To best simulate unpolarized light, the simulations were done for both s- and p-polarized light and the average of these was used. In the initial simulations, parameters like period, that is, the distance between particles, and thickness of the oxide layer, explained in further detail in sections 4.1.6 and 4.1.4, was to be determined. In these simulations, it was sufficient to use p-polarized light due to the incident light angle, which will be explained in the next section.

4.1.3 Incident Light Angle

The aim was to simulate the response of the system to diffuse light, that is, angled illumination. The angle of the incident light ranged from 0 to 55° relative to the surface normal, with a 5° interval step. The light angle relative to the particle array is illustrated in fig. 4.1. Because of the pyramidal textured surfaces of the PV cells, with a base angle of 54.74° (see section 1.4.1), it was not necessary to simulate angles steeper than 55°. As mentioned in the previous section, the period and oxide layer thickness were determined in the first simulations. To save time, these simulations were performed using p-polarized light illuminating at only one angle. The angle chosen was 20° as this is a diffuse light angle where there is little difference in reflection between p-, s- and unpolarized light, as can be seen in fig. 1.6.

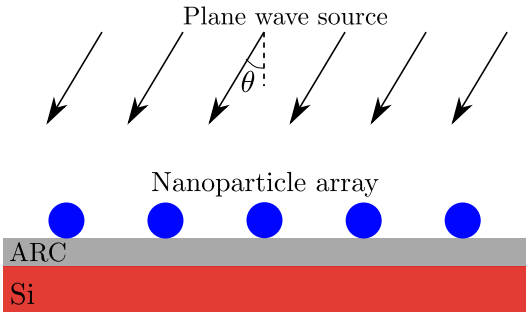

Figure 4.1: An illustration of the incident light angle θ relative to the surface normal and the particle array, seen from the side.

4.1.4 Nanoparticle Material

When deciding on the nanoparticle material to simulate there are two major considerations. The material used must be present on Earth in a large enough quantity to be used for large enough areas at a reasonable price. The amount of each element on Earth is finite, meaning that overconsumption could result in a short supply of the elements. Elements facing limited supply are all the rare earth elements, but also elements such as gallium (Ga) and silver (Ag), the former being a much-used alternative to Si in thin film PV cells, while research is done on how to utilize the latter in plasmonic PV cells, as described in section 1.4.3 [52, 53]. Even though Ag nanoparticles have shown promising effects in plasmonic PV cells, the fact that Ag is an "endangered" element makes it inappropriate on a large scale. The same applies to gold (Au), and other materials must be considered. Besides, both Au and Ag are expensive materials and using them in PV cells would be costly. However, it is of course not only the abundance and price that matters. The second major consideration is that the addition of nanoparticles to the PV cell must lead to a significant increase in efficiency. Al is the seventh most abundant material on Earth. While the Earth consists of only 0.16 and 0.05 ppm Au and Ag by mass, respectively, 15 900 ppm, or 1.59 %, of the Earth's mass is Al. This is more than 10^5 times as much as Au and Ag [54]. The abundance of Al makes it a cheap material. In addition, Al nanoparticles have shown promising effects for the use in plasmonic PV cells (see section 1.4.3). Based on this, different configurations of Al were simulated in this thesis work.

Oxide Layer

As described in section 1.4, spherical core-shell nanoparticles with a metal core and a dielectric shell are promising forward scatterers. Al nanoparticles oxidize spontaneously when in air, and the thickness of the native oxide layer is 2 to 6 nm [55]. Thus, the nanoparticles naturally become core-shell particles with an Al core and alumina (Al_2O_3) shell. Further oxidation of Al is also possible, and simulations were the thickness of the oxide layer increased were performed to decide on which thickness was best.

4.1.5 Nanoparticle Size

When deciding on which nanoparticle sizes to simulate, results from the literature were used. As discussed in section 1.4.3, Zhang et al. [27] did both simulations and experiments on spherical Al nanoparticles on top Si PV cells. They measured the transmission into Si with particles of diameters 100, 200 and 300 nm with a 300 to 1200 nm wavelength interval. The smallest particle diameter gave an increase in transmission over the whole wavelength interval, being highest for shorter wavelengths, 300 to 600 nm, and then flatting out for longer wavelengths. The particle diameters 200 and 300 nm gave low transmission for the shorter wavelengths before it increased rapidly at around 580 and 800 nm, respectively. They also found that particles of diameter 150 nm and 30 % surface coverage gave the largest enhancement in transmission. Since diffuse light is more intense

in the blue-green spectral region, it was of interest to optimize the transmission in this region, making the smaller nanoparticles more interesting. In addition, nanoparticles in this diameter range could be synthesized at Rice University [56]. Therefore, nanoparticles with diameters 100, 120 and 140 nm were simulated.

4.1.6 Period

The simulations performed used a broadband light source under angled illumination. Therefore, BFAST had to be used such that the light angle did not change with frequency, as described in section 2.3. BFAST has built-in periodic boundary conditions. Consequently, the configuration of the nanoparticles had to be periodic. This could lead to diffraction via far-field coupling for large periods, which impacts the transmission into Si. Near-field coupling between the nanoparticles could also occur if they were closely spaced, resulting in a shift of the LSPR that also impacts the transmission. Both of these phenomena are discussed in section 2.2.4. It was therefore important to simulate with different periodicity to see how the transmission into Si was impacted, and thereafter choose the period giving the best results.

Overview of the Parameter Space

Substrate	Flat Si slab coated with 80 nm thick Si_3N_4 layer
Wavelength Range	300 - 900 nm
Incident Light Angle	0° - 55°, 20° for initial simulations
Nanoparticle Material	Spherical Al nanoparticles coated with Al_2O_3
Nanoparticle Size	100 - 140 nm, thickness Al_2O_3 3 nm (fig. 4.8)
Period	Three times the diameter of the nanoparticles (fig. 4.5)

Table 4.1: Overview of the parameter space.

4.2 Simulation Results

4.2.1 Scattering and Absorption Cross Sections for Al Nanoparticles With Oxide Layer

The absorption and scattering cross sections for Al nanoparticles with diameters 100, 120 and 140 nm and a 3 nm oxide layer are presented in figs. 4.2 and 4.3, respectively. There is a distinct resonance peak in both the scattering and absorption cross section for all three nanoparticles. In the absorption cross section, both the 100 and 120 nm nanoparticles

resonate at approximately 365 nm, while the resonance of the 140 nm nanoparticle is slightly red-shifted to approximately 410 nm. The magnitude of the absorption increases with particle size, except for the shortest wavelengths, where the 120 nm nanoparticle absorbs the most.

In the scattering cross section, the 100 nm nanoparticle resonates at around 340 nm, while the resonance red-shifts to 370 nm and 400 nm for the 120 and 140 nm nanoparticles, respectively. The scattering gets stronger as the nanoparticle diameter increases. The resonance peak also broadens as the diameter increases. Note that the scattering cross section changes more with nanoparticle size than the absorption cross section, as is expected from eqs. 2.27 in chapter 2.

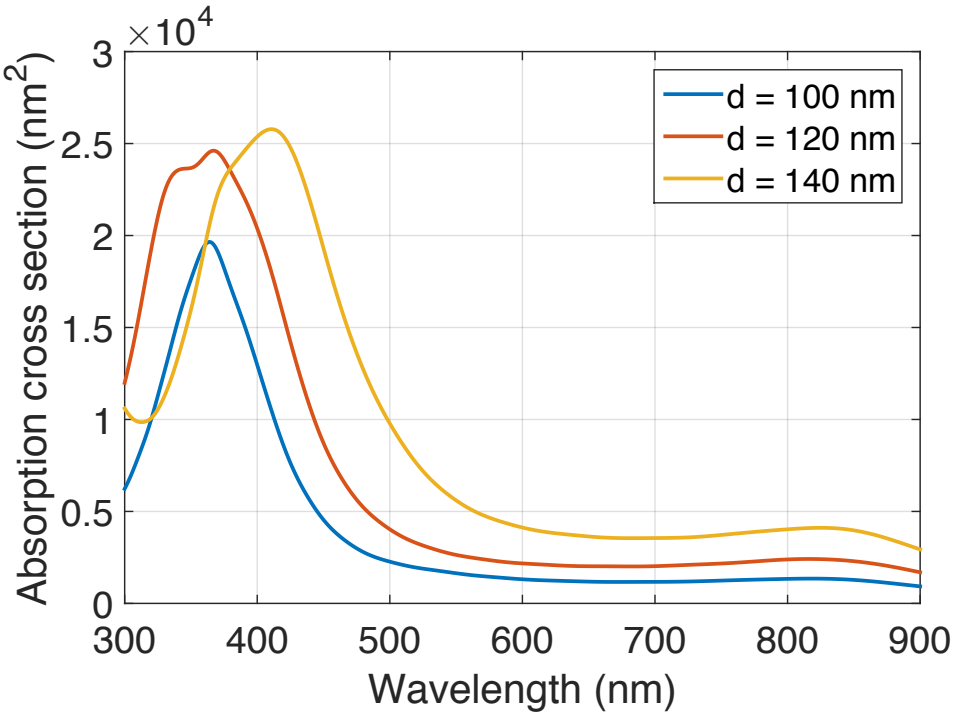

Figure 4.2: The absorption cross sections of Al nanoparticles with diameters 100, 120 and 140 nm and a 3 nm oxide layer on top of a flat Si_3N_4 coated Si slab.

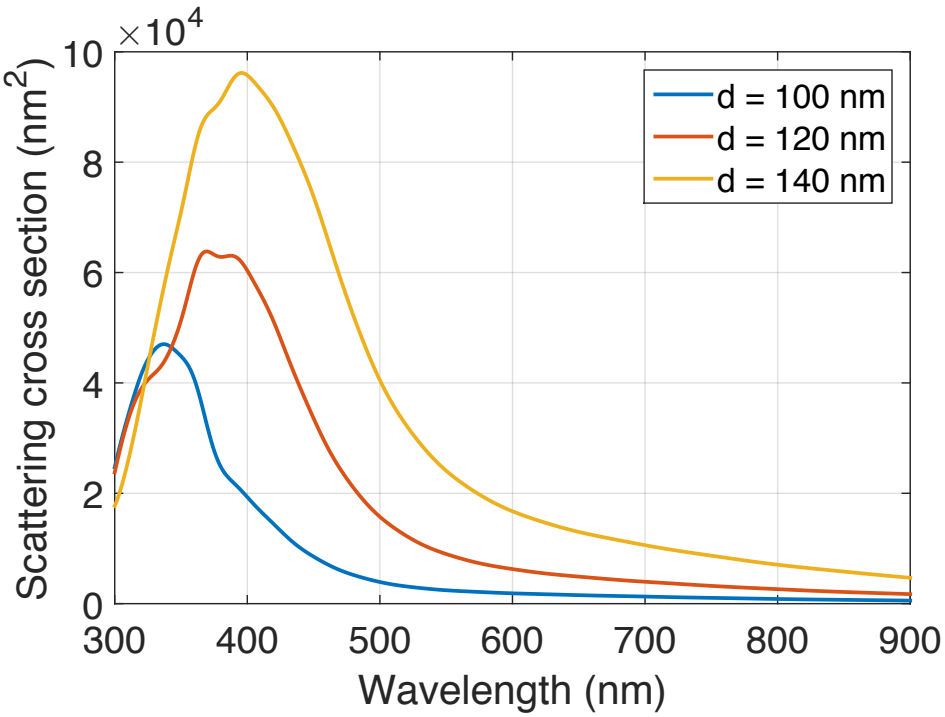

Figure 4.3: The scattering cross sections of Al nanoparticles with diameters 100, 120 and 140 nm and a 3 nm oxide layer on top of a flat Si_3N_4 coated Si slab.

4.2.2 Reproducing Results From the Literature

Results from Zhang et al. [27] were reproduced to verify that the simulation setup functioned correctly. The results reproduced was the transmission into Si with and without Al nanoparticles with 10 % surface coverage on top. The results are presented in fig. 4.4. It is clear that all the reproduced results follow the same trend as the original results. The exception is for the shortest wavelengths, around 300 to 400 nm, where the reproduced results give a lower transmission. It is not clear why this happens. The simulation parameters in the reproduced results are as far as possible the same as in the original results. However, it is not clear in the description of the simulation setup by Zhang et al. how deep into the Si slab the monitor measuring the transmission was placed. In addition, Lumerical has two Al material databases which are slightly different. Zhang et al. do not specify which alternative they have used. Both these aspects could affect the transmission results. In the reproduced results the transmission was measured 20 nm into the Si and the "Al (Palik)" material database was chosen [57]. In the analysis of the simulation results in the next sections, the wavelength region where the results differ was disregarded.

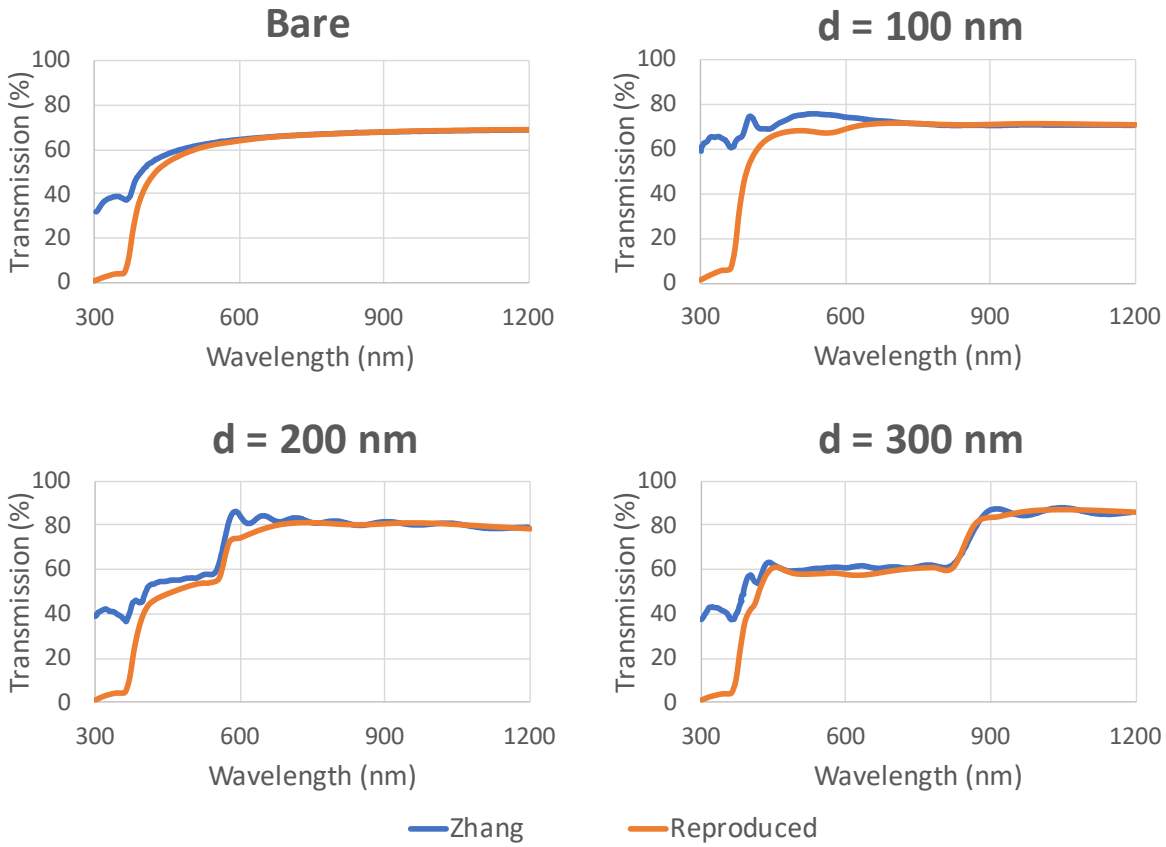

Figure 4.4: The original and reproduced results from Zhang et al. The reproduced results follow the same trend as the original results, except for the shorter wavelengths (300 to 400 nm). The reproduced results contain fewer fluctuations because fewer data points were collected to save time during the simulations.

4.2.3 Simulating With Different Periodicity

The first simulations were done with fixed light angle and size of the nanoparticles while varying the period. The period ranged from 150 to 400 nm. The light injection angle was 20° relative to the surface normal and the nanoparticle diameter was 100 nm. The oxide thickness was 3 nm, since that is a native oxide thickness. Fig. 4.5 shows the results, including the transmission when no nanoparticles are present for comparison. All periods show low transmission from 300 to 370 nm, followed by a continuous rise that flattens out asymptotically to a transmission of approximately 0.94. The low transmission from 300 to 370 nm is most likely an artifact, as was seen when reproducing the results of Zhang et al. in the previous section. Note that the transmission when no nanoparticles are included (blue line) is lower for all wavelengths, except for the shortest period, which shows an increase between 430 to 560 nm followed by lower transmission than all between 590 to 880 nm. The largest and second-largest periods show a decrease in transmission

between 420 to 520 nm and 420 to 465 nm, respectively. However, the transmission is still higher than the transmission with no nanoparticles.

The curves all follow a characteristic path, which might be due to the refractive index of Si. The refractive index of Si increases from 5.0 to 6.7 between 300 to 375 nm before it rapidly decreases to 4.3 at 500 nm and continues to decrease more slowly for longer wavelengths [58]. This coincides with the sharp rise at around 375 nm. The low transmission between 300 to 400 nm could also be due to an artifact in the simulations in this region, as already mentioned.

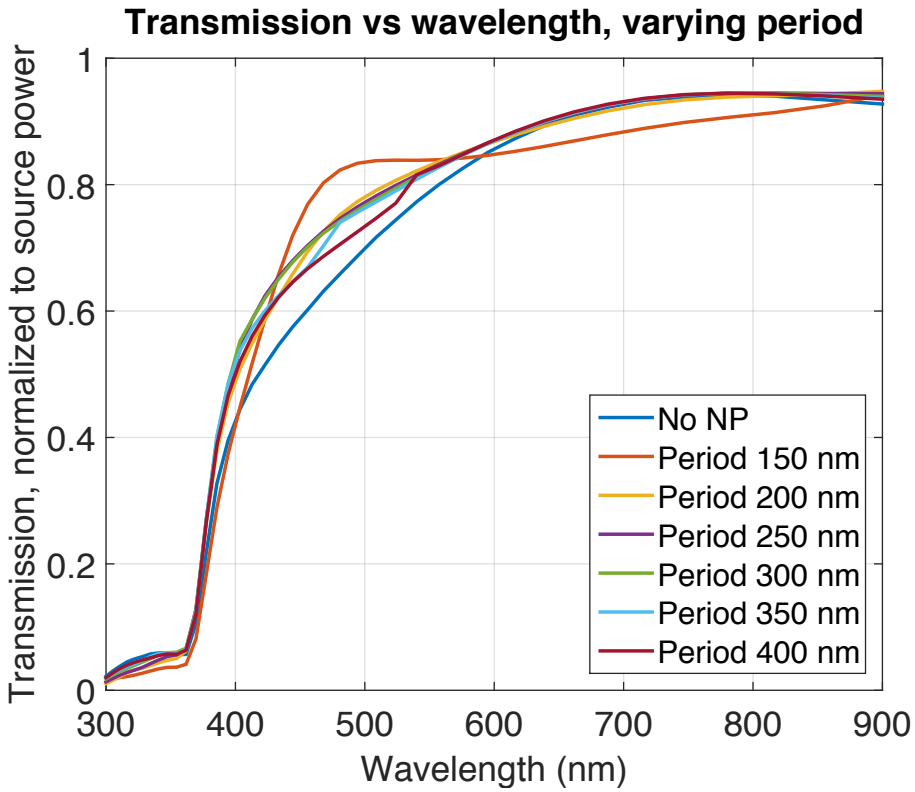

Figure 4.5: The simulation results for Al nanoparticles of diameter 100 nm and varying period. The injection angle relative to the surface normal was 20° and the light was p-polarized. The shortest period (orange line) shows a higher transmission between 430 to 560 nm than all the other periods and a lower transmission than all between 590 to 880. This is most likely due to near-field coupling between the nanoparticles.

The deviation for the smallest period (orange line) between 430 to 560 nm and 590 to 880 nm is probably a result of near-field coupling between the nanoparticles which affects the LSPR of the nanoparticles. The largest period (red) shows a reduction in transmission from 420 nm ending with a kink at 520 nm. This also happens for the second-largest period, which shows a reduction from 420 nm ending with a kink at 465 nm. These reductions could be due to far-field coupling between the nanoparticles via diffraction since they are in a periodic array, as discussed in section 2.2.4. To examine this, the reciprocal lattices of the nanoparticle arrays for both periods were calculated, as

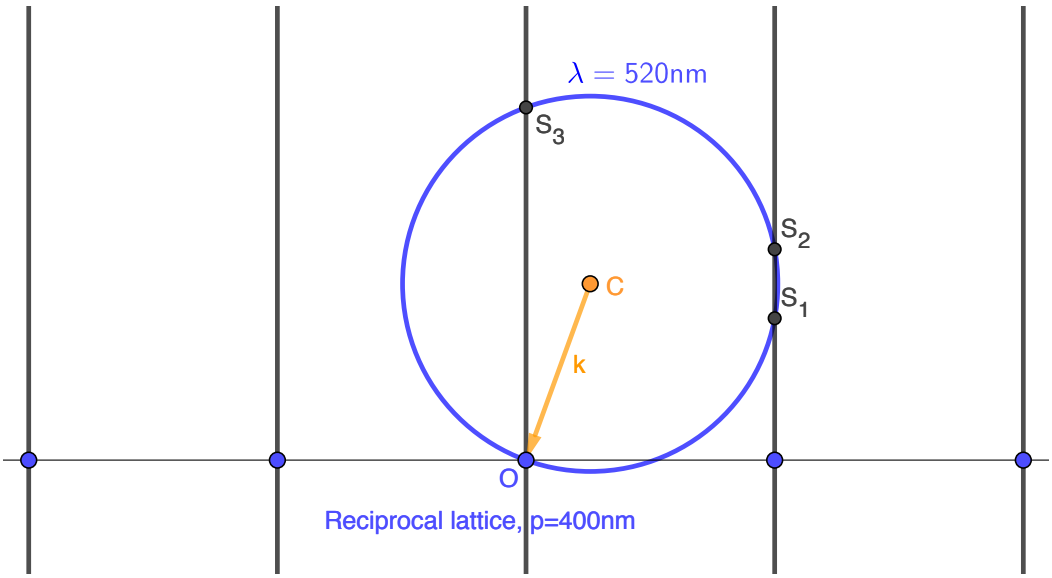

Figure 4.6: The reciprocal lattice for the nanoparticle array with period 400 nm. The k-vector, incident 20° relative to the surface normal, and Ewald sphere are drawn for the wavelength 530 nm, where the reduction in transmission ends. The diffraction from the point S_1 will be visible when measuring the transmission.

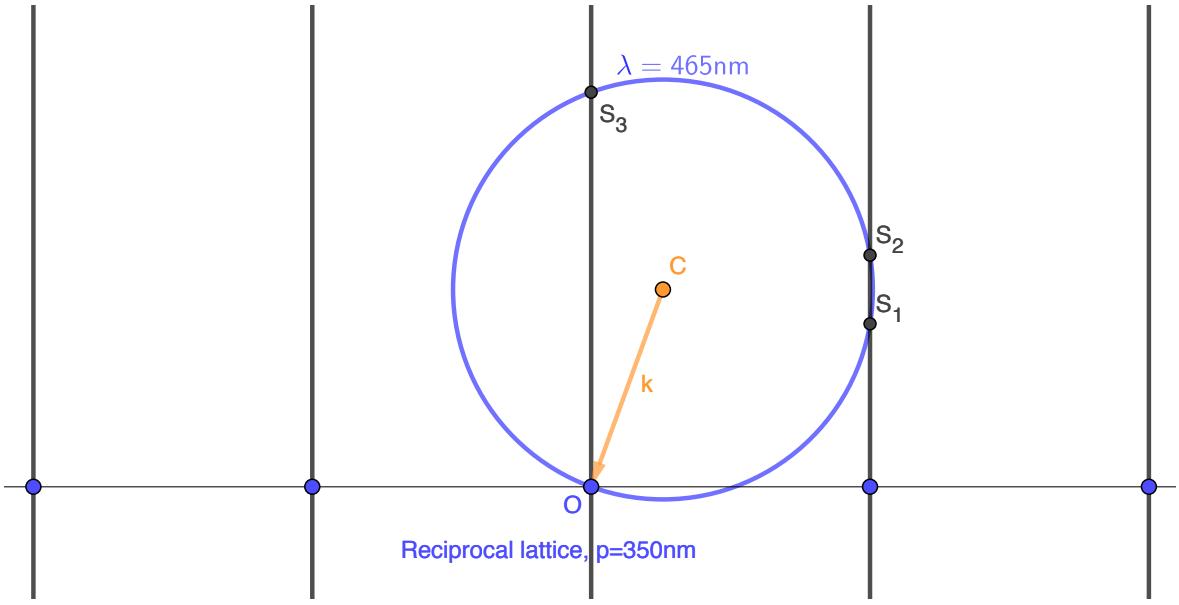

Figure 4.7: The reciprocal lattice for the nanoparticle array with period 350 nm. The k-vector, incident 20° relative to the surface normal, and Ewald sphere are drawn for the wavelength 465 nm, where the reduction in transmission ends. Again, the diffraction from the point S_1 will be visible when measuring the transmission.

well as the k-vectors (wave vectors) of the incident light for the wavelengths at the kinks (520 and 465 nm). An Ewald sphere was drawn for each period and are shown i figs. 4.6

and 4.7. The k-vectors are incident at 20° relative to the surface normal of the reciprocal lattice since the light injection angle was 20°. For diffraction to occur, Bragg's law must be fulfilled, which is the case when the Ewald sphere intercepts the reciprocal rods [59]. Hence, diffraction occurs for the points S_1 for both periods in the forward direction where the transmission is measured. The diffracted waves have most likely interfered with the scattered waves resulting in destructive interference.

Based on the above discussion, on the rest of the simulations on Al nanoparticles, the period was three times longer than the size of the nanoparticles, as this is a period that maximizes the transmission over all wavelengths from 300 to 900 nm.

4.2.4 Simulating With Different Thickness of Oxide Layer

To see how the thickness of the oxide layer impacted the transmission, Al nanoparticles of diameter 120 nm with different oxide thicknesses were simulated. Again, the injection angle relative to the surface normal was 20°. The results, presented in fig. 4.8, show that the thinner oxide layer is clearly better than a pure Al nanoparticle and gives the highest transmission. Even a fully oxidized Al nanoparticle leads to an improvement in transmission. The fact that the thinner oxide layer gives the highest transmission is favorable regarding fabrication since it is within the interval of the native oxide thickness. Based on these results, the rest of the simulations on Al nanoparticles were done with a 3 nm oxide layer.

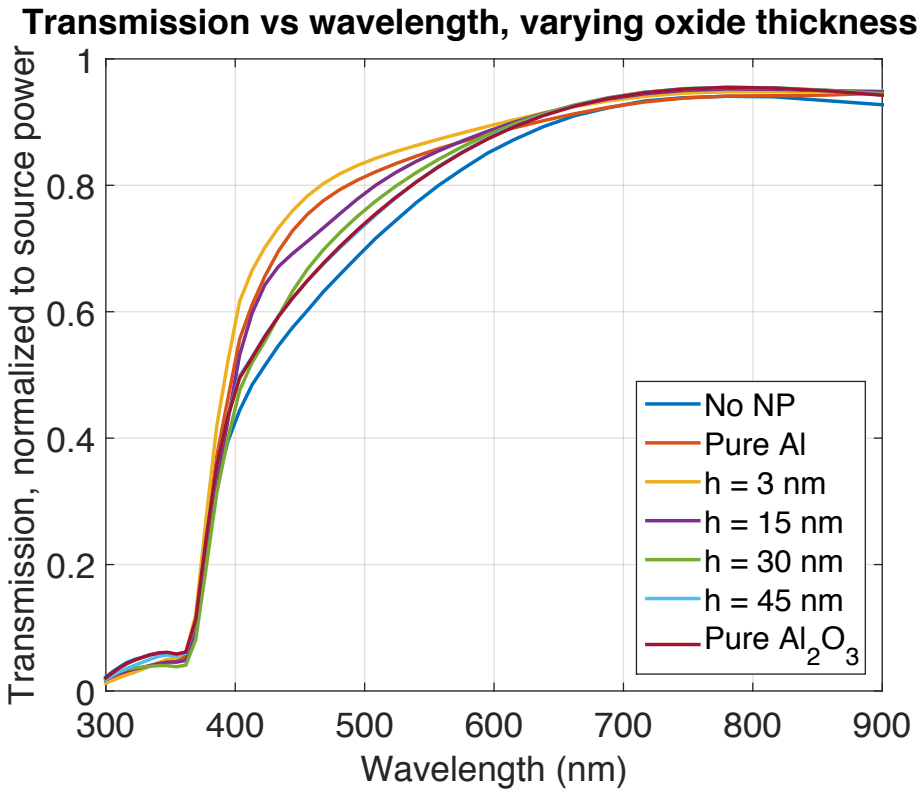

Figure 4.8: The simulation results for Al nanoparticles of diameter 120 nm and varying thickness of the oxide layer, ranging from a pure Al nanoparticle to a fully oxidized nanoparticle. The injection angle was 20° relative to the surface normal and the light was p-polarized. The transmission is highest with a thin oxide layer, but even for a fully oxidized Al nanoparticle, there is an improvement in transmission.

4.2.5 Simulating With Varying Incident Light Angle and Diameter of Nanoparticles

Finally, simulations where three different diameters of the Al nanoparticles with a 3 nm oxide layer (later referred to as only Al nanoparticles) were added to the substrate, as well as no nanoparticles added, were done while varying the angle from 0 to 55° with an interval step of 5°. The results for both p- and s-polarized light are presented in figs. 4.9 to 4.12.

For p-polarized light, figs 4.9 and 4.10, all configurations show low transmission between 300 to 370 nm before a continuous increase in transmission for all angles. From 0° to 25° a continuous rise in transmission that flattens at longer wavelengths (approximately 650 nm) follows for all configurations. The transmission when no nanoparticles are added (blue line) is lower for all wavelengths and angles in this interval. From 0° to 10° the nanoparticles with diameter 140 nm gives the highest transmission, while nanoparticles with diameter 120 nm give the highest transmission from 15° to 25°. At 30° a feature

is appearing at approximately 440 nm for all the diameters. The features increase and red-shift as the angle gets steeper. In this region the transmission with nanoparticles decreases, and at 45° it is below the transmission when no nanoparticles are added for all the diameters. It is not clear what happens here, but it seems like it only depends on the incident light angle and the wavelength of the light, and not the diameter of the nanoparticles.

All configurations show low transmission between 300 to 370 nm also for s-polarized light. This is followed by a continuous rise before the curves flatten at longer wavelengths. This applies to all angles and configurations. Note that the feature seen for p-polarized light is not seen for s-polarized light. For the smallest angles, there is a feature for the largest diameter (purple line) which gets less and less apparent before it completely disappears at 20°. The feature appears again when the incident light angle is 45°. Apart from this feature, the transmission is slightly higher with nanoparticles of diameter 140 nm than diameters 100 and 120 nm for angles 0° to 15° and 40° to 55°. For the angles in between, the transmission with nanoparticles with diameters 120 and 140 nm is approximately equal while the transmission for nanoparticles with diameter 100 nm is slightly lower. The transmission when no nanoparticles are added is lower for all wavelengths and angles. For both s- and p-polarized light the increase is especially high between 400 to 600 nm where diffuse light has its highest intensity, making the results even more interesting.

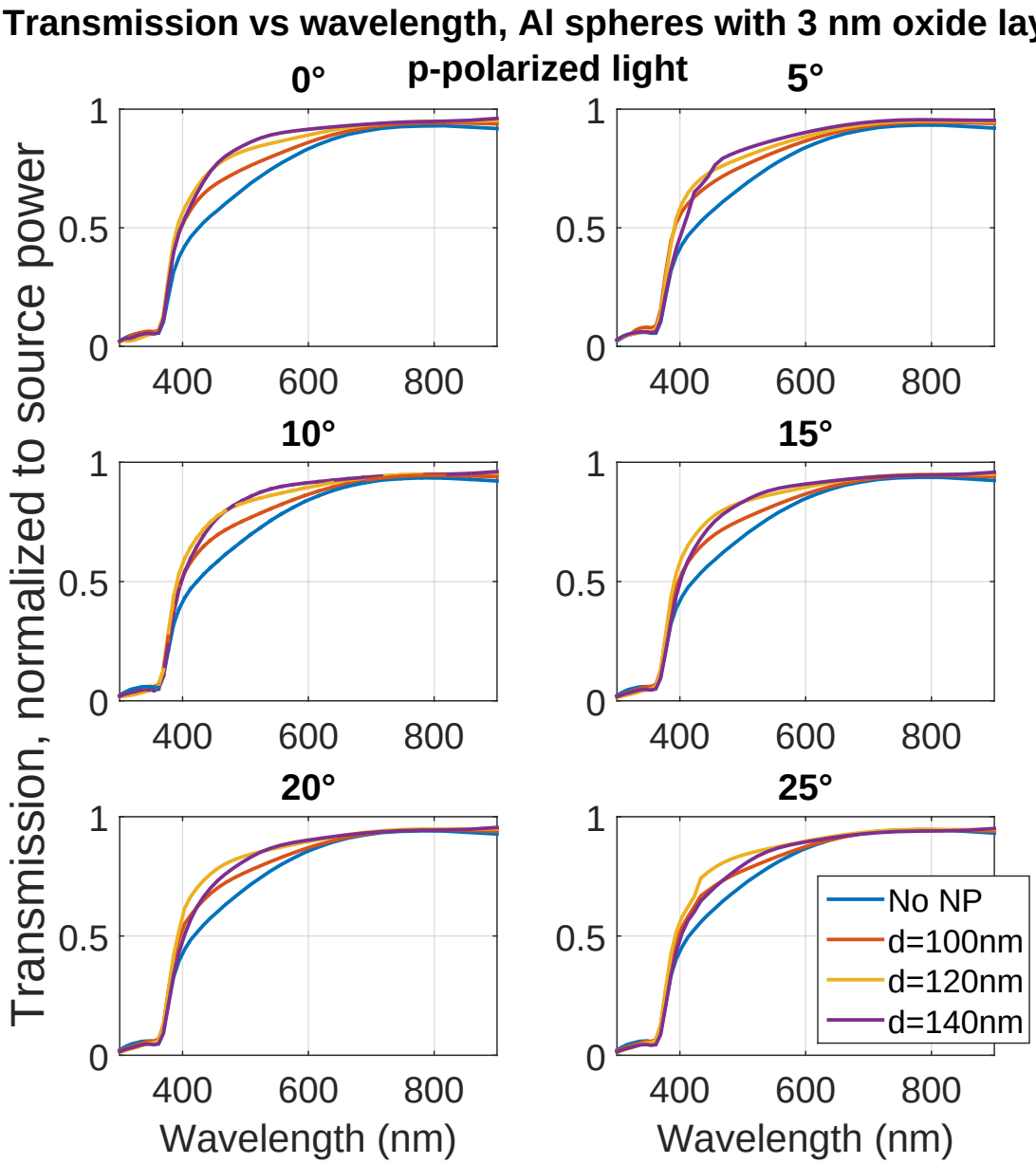

Figure 4.9: The simulation results for Al nanoparticles of three different sizes with a 3 nm thick oxide layer and incident angle of light from 0-25° relative to the surface normal. The light was p-polarized. There is a significant improvement in transmission of blue-green light for all three sizes of the nanoparticles compared to the transmission when no nanoparticles are added on top of the cell. The improvement decreases as the angle increases.

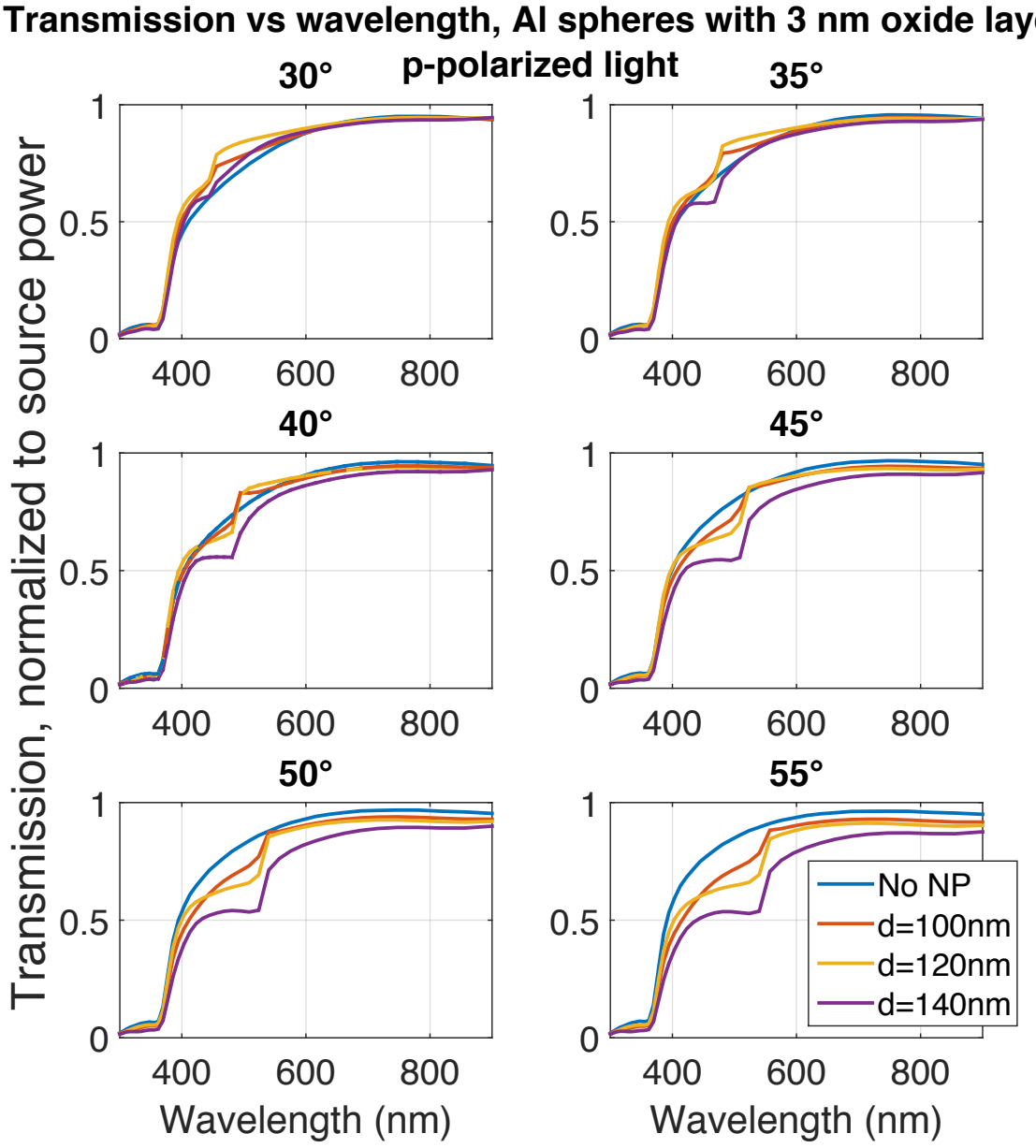

Figure 4.10: The simulation results for Al nanoparticles of three different sizes with a 3 nm thick oxide layer and incident angle of light from 30-55° relative to the surface normal. The light was p-polarized. When the injection angle of the light exceeds 35° there is no longer an increase in transmission when the Al nanoparticles are introduced.

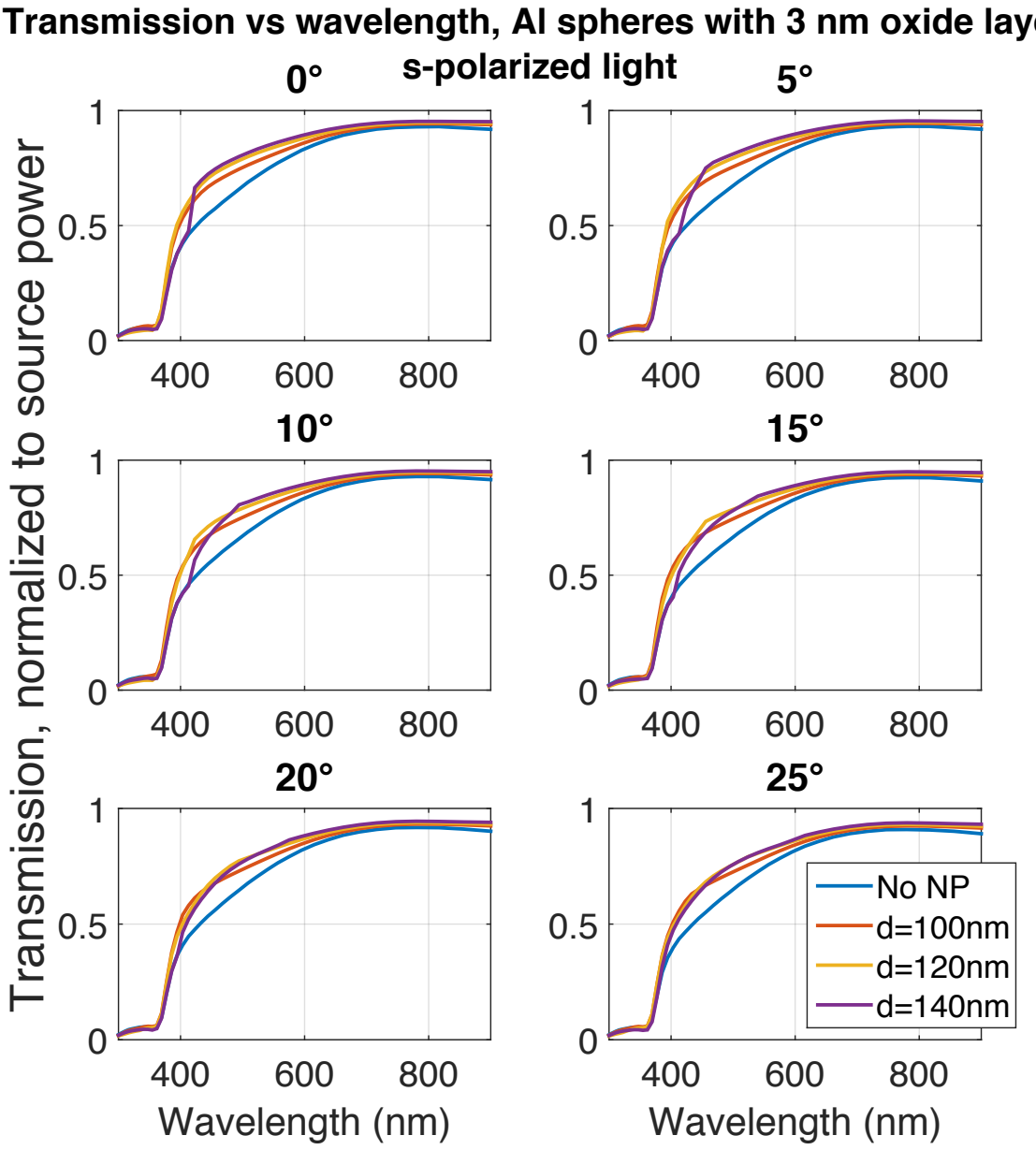

Figure 4.11: The simulation results for Al nanoparticles of three different sizes with a 3 nm thick oxide layer and incident angle of light from 0-25° relative to the surface normal. This time, the light was s-polarized. Again, there is a significant improvement in transmission of blue-green light for all three sizes of the nanoparticles compared to the transmission when no nanoparticles are added on top of the cell.

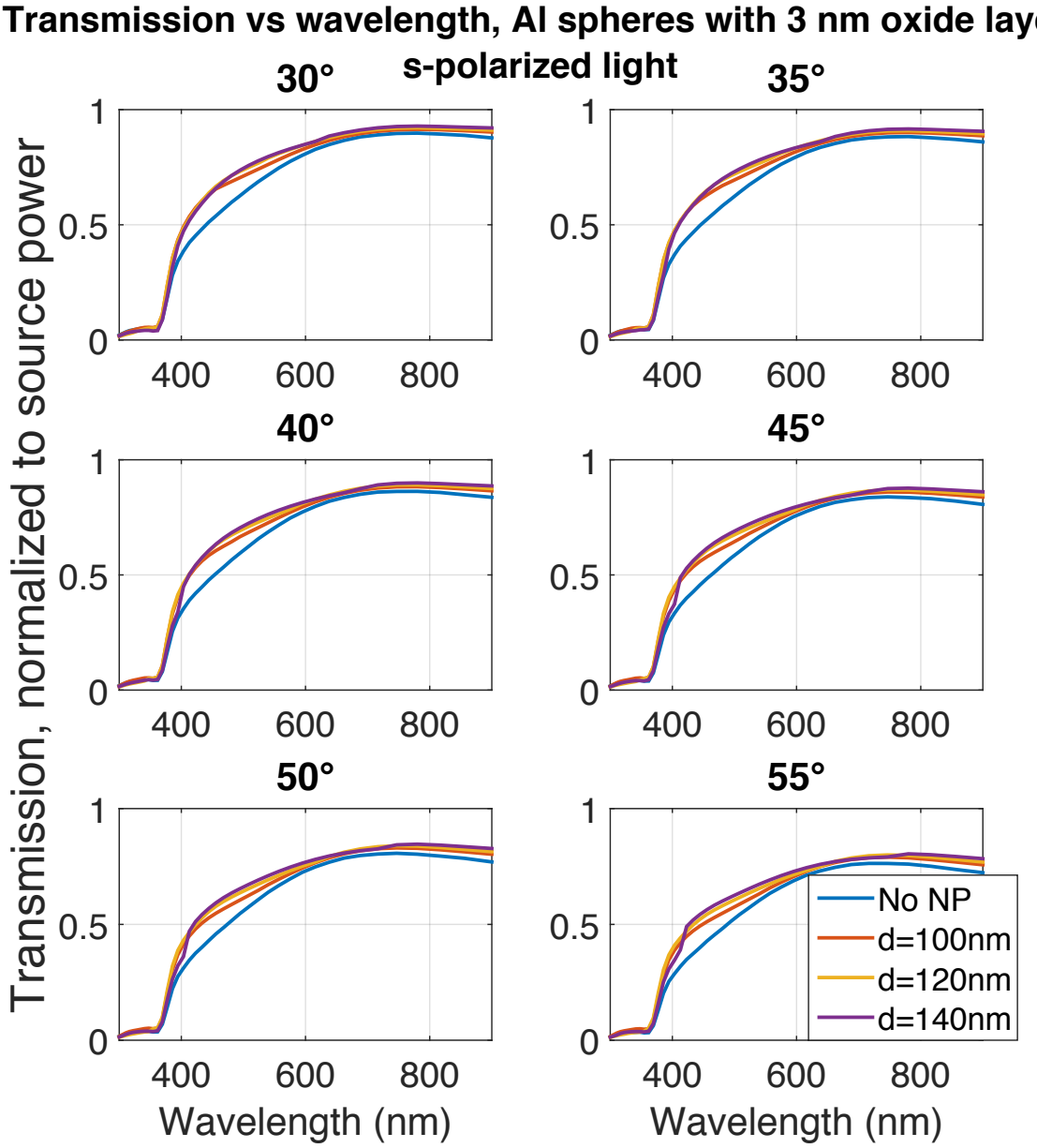

Figure 4.12: The simulation results for Al nanoparticles of three different sizes with a 3 nm thick oxide layer and incident angle of light from 30-55° relative to the surface normal. For s-polarized light, the transmission is still increased at steeper angles, in contrast of the transmission for p-polarized light.

4.2.6 Simulating With Aluminum Disks

In case planar fabricated nanodisks could be used, simulations using Al nanodisks of various sizes on top of the ARC coated Si slab were also done. These disks can be easily fabricated using electron beam lithography (EBL). The wavelength range was again 300 to 900 nm.

The first simulations were done with an incident light angle of 20°. The height and period were changed one at a time while keeping the diameter constant at 30 nm. The diameter was chosen due to its easy fabrication. First, the height was held constant at 30 nm and the period varied from 60 to 240 nm, with a 30 nm interval, equal to one disk diameter. As long as the period was greater than or equal to three times the diameter of the disk the transmission was not much affected. For the smallest period, there was a decrease in transmission for wavelengths 420 nm and longer. As with spherical nanoparticles, this is probably due to near-field coupling between the nanoparticles, which results in a shift of the LSPR, as described in section 2.2.4. Secondly, the height of the disks was varied from 30 to 80 nm, with a 10 nm interval, while keeping the period constant at 90 nm. The transmission stayed the same for the heights from 30 to 70 nm, while a small decrease was observed when the height was 80 nm. Based on these results, the period was set to be three times the diameter of the nanodisks in the rest of the simulations, and the height was chosen based on what is easiest to fabricate.

Finally, simulations were done where the height was kept constant and the diameter varied. The period was always three times greater than the diameter and the height was 15 nm. These simulations were done with the same angles of the incident light as for the spherical Al nanoparticles. Some of the results are presented in fig. 4.13 and, as is clear from the results, all sizes lead to a decrease in transmission compared to when no nanoparticles were added (blue line), with the largest decrease for the largest nanoparticles. The transmission is only slightly lower with the addition of the smallest nanoparticles (orange line). This is a sign of Al nanodisks not being as good forward scatterers as Al nanospheres.

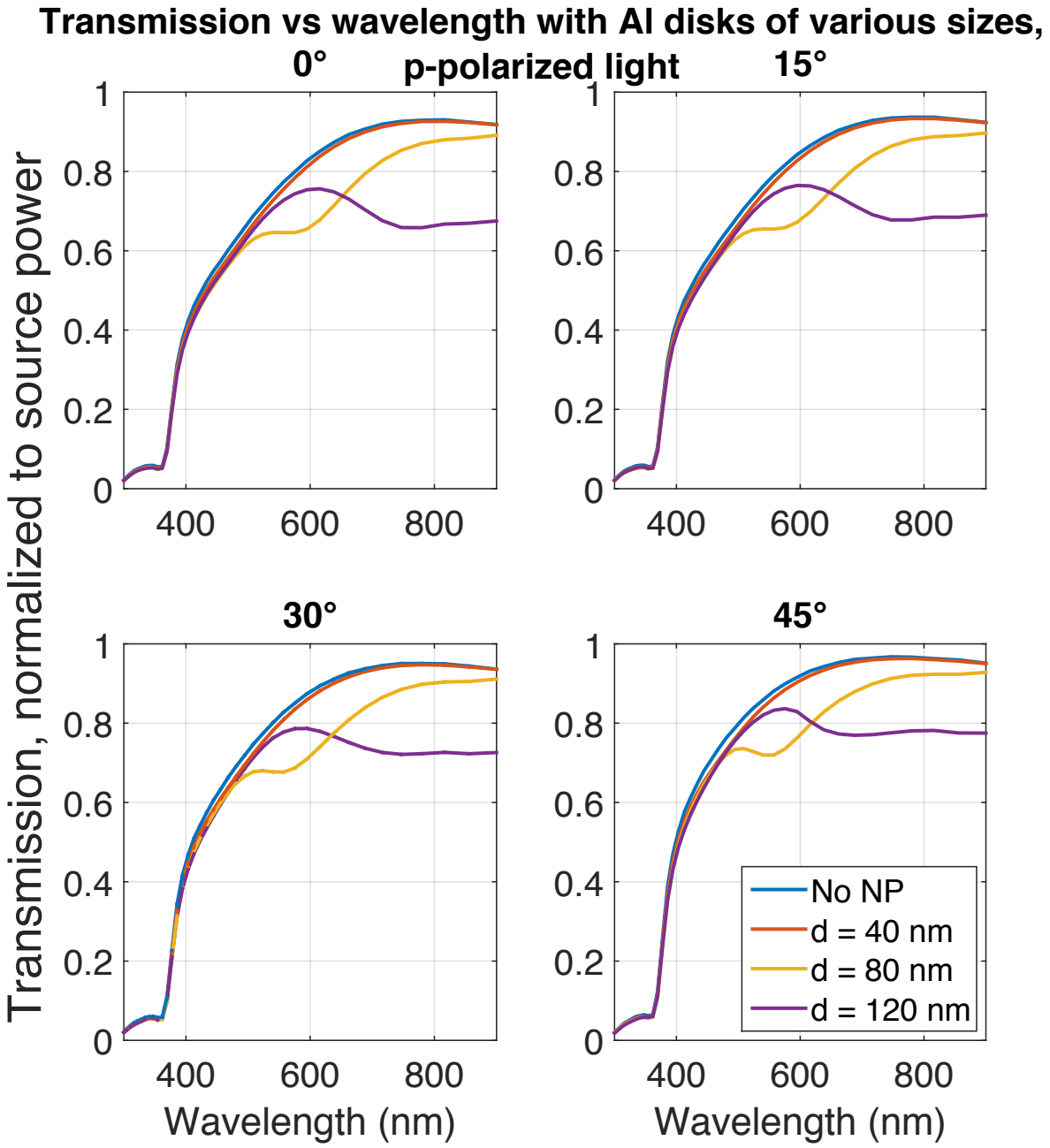

Figure 4.13: The simulation results for Al nanodisks of three different sizes and light incident at angles from 0-45°. The light is p-polarized. All the sizes lead to a decrease in transmission.

4.3 Total Increase In Transmission When Adding Spherical Aluminum Nanoparticles

To find the overall increase in transmission over the whole wavelength interval and all angles, the average of the transmission of unpolarized light, that is, the average of the s- and p-polarized transmission, over all wavelengths and angles was calculated. This was done for all the three nanoparticle sizes separately and for the results with no nanoparticles. Then, the percentage increase for each size of the nanoparticles was found. Since there might be an artifact in the light incoupling results between 300 to 400 nm, as discussed in section 4.2.2, the results from these wavelengths were omitted and the wavelength interval was 400 to 900 nm. The overall increase in transmission was also calculated for a shorter wavelength interval, where the diffuse light intensity is highest, between 400 to 600 nm (see fig. 1.2). The results are presented in table 4.2. In both wavelength intervals, the increase in transmission was highest when nanoparticles of diameter 120 nm were added.

Total Increase in Transmission

	Wavelengths 400 - 900 nm	**Wavelengths 400 to 600 nm**
d = 100 nm	4.93 %	8.64 %
d = 120 nm	7.46 %	12.91 %
d = 140 nm	4.65 %	7.89 %

Table 4.2: An overview of the total increase in transmission over all incident light angles when adding Al nanoparticles with respect to no addition of nanoparticles. The addition of Al nanoparticles of diameter 120 nm leads to the highest increase in transmission both over the whole wavelength interval and the shorter interval where the intensity of diffuse light is highest. The period was three times the diameter of the nanoparticles.

The change in transmission over all wavelengths for the various incident light angles was also calculated for all three diameters of the nanoparticles. The results are presented in table 4.3 and fig. 4.14. The trend is the same for all the diameters. For small angles, there is a relatively large increase in transmission that gradually becomes smaller as the angle increases, and finally, negative for the two (three for d = 140 nm) steepest angles. The largest nanoparticle has the steepest (negative) slope (purple curve), while the smallest nanoparticle decreases more slowly (yellow curve). In general, nanoparticles of diameter 120 nm gives the highest transmission, except for 0° and 55°, where the transmission with nanoparticles of diameter 140 and 100 nm, respectively, is slightly higher.

Change in Transmission With Angle

Angle	d = 100 nm	d = 120 nm	d = 140 nm
0°	8.21 %	12.73 %	12.86 %
5°	8.52 %	11.95 %	11.01 %
10°	7.99 %	12.37 %	11.21 %
15°	7.74 %	11.79 %	10.95 %
20°	7.47 %	11.13 %	8.95 %
25°	6.88 %	10.06 %	7.69 %
30°	5.98 %	8.53 %	5.84 %
35°	4.67 %	6.58 %	3.41 %
40°	3.21 %	4.60 %	0.66 %
45°	1.31 %	2.18 %	-2.49 %
50°	-0.56 %	-0.12 %	-5.36 %
55°	-2.58 %	-2.59 %	-8.52 %

Table 4.3: An overview of the change in transmission over all wavelengths for each angle, measured relative to the surface normal, when adding Al nanoparticles with respect to no addition of nanoparticles.

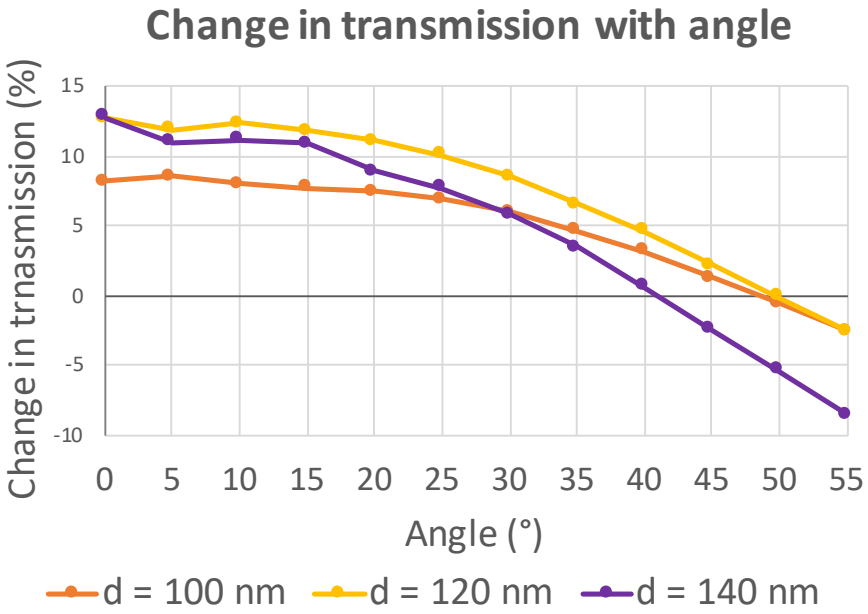

Figure 4.14: The change in transmission over all wavelengths with angle, measured relative to the surface normal. The increase in transmission is largest with the addition of the nanoparticle of diameter 120 nm.

The simulations were all done on flat surfaces, but as mentioned in the beginning of the chapter, textured surfaces are usually used on commercial PV cells (see section 1.4.1). If the nanoparticles are going to be added on top of structured PV cells, the results have to be analyzed with this in mind. An incident light angle of 0° relative to the surface normal in the simulations corresponds to an incident angle of approximately 55° relative to the surface normal of a structured PV cell, an angle of 5° in the simulations corresponds to an angle of 50° on a structured PV cell and so on. This is illustrated in fig. 4.15. Thus, the transmission for solar radiation incident normal to the PV cell surface is lower when adding nanoparticles. However, it is reasonable to assume that most of the light that is not transmitted is scattered onto the cell surface at some other place and hits the surface with a smaller angle (see fig. 1.4). More of this light will then be transmitted than if no nanoparticles are added, and since the increase in transmitted light is larger for small angles than the decrease for steep angles, more light will be transmitted into the PV cell in total.

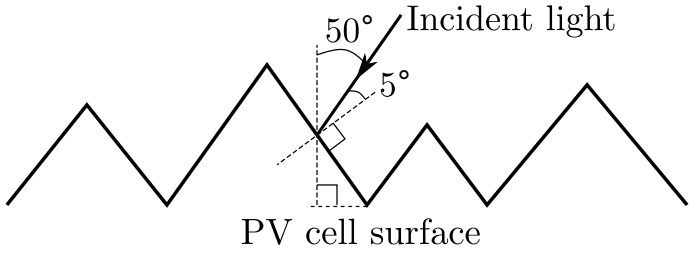

Figure 4.15: The illustration shows how the angles used in the simulations will represent a different incident light angle if the nanoparticles are placed on top of a structured PV cell. Here illustrated with an incident light angle of 5° relative to the surface normal of the pyramids, which represents an incident light angle of 50° relative to the surface normal of the PV cell.

4.4 Overall Increase in PV Cell Efficiency

The true efficiency of a PV cell is determined by the transmission for each wavelength multiplied by the conversion efficiency and weighted against the solar spectrum distribution. The highest theoretical efficiency that can be achieved is given by the Shockley-Queisser Limit, described in detail in section 2.1.3. The Shockley-Queisser Limit is given by eq. 2.7, repeated here

$$\eta_{max} = \text{ff} \times \frac{eV_{oc}}{E_{gap}} \times \eta^{max}_{collection}$$

The first two terms on the right-hand side of the equation only depend on the properties of the PV cell material, while the last term also depends on the energy and intensity of the incident light, that is, the solar spectrum. For an ideal Si PV cell, $\text{ff}_{max} \approx 0.87$, $eV_{oc}/E_{gap} \approx 0.774$ and $\eta^{max}_{collection} \leq 0.49$, resulting in a maximum theoretical efficiency of

33 %. To make a simplified model to calculate the change in efficiency when introducing nanoparticles on top of a Si PV cell, suppose illuminating a Si PV cell with ideal material properties, and overall efficiency 33 % when an energy equal to E_{gap} from all incident photons with energy $E \geq E_{gap}$ ($\cong$ 1.1 eV for Si) is collected (see section 2.1.3). The above expression can then be used to calculate the efficiency. The first two terms could be held constant since these terms will not change when introducing nanoparticles on top of the PV cell. Only the last term varies with the addition of nanoparticles. Since the material properties are ideal, the product C of the first two terms becomes

$$\mathrm{C} = \mathrm{ff} \times \frac{eV_{oc}}{E_{gap}} \approx 0.87 \times 0.774 = 0.67338 \approx 0.67 \tag{4.1}$$

Thus, the overall efficiency η_{eff} of the PV cell is given by

$$\eta_{eff} = \mathrm{C} \times \eta_{collection} = 0.67\ \eta_{collection} \tag{4.2}$$

The first step to calculate the efficiency is then to find $\eta_{collection}$ for all the different configurations simulated. The efficiency calculations were done for the results in the wavelength region 400 to 900 nm for the same reasons as when calculating the total increase in transmission (see section 4.3). In this wavelength region, all photons have energies greater than the bandgap of Si, as described in section 4.1.2. First, the total incident energy in this region was calculated. The intensity of the light at the different wavelengths was found using the AM1.5 solar spectrum (data from [60], see fig. 1.2) and then multiplied by the energy of the light at each wavelength. Perfect diffuse light was assumed, meaning that the same amount of light was incident at all angles. Then, the amount of energy transmitted into the Si slab was calculated. The amount of transmitted light was weighted to the AM1.5 spectrum and then multiplied by 1.1 eV, assuming that the maximum energy that can be extracted from each photon was extracted. This was done for all angles before taking the average over all angles. Finally, eq. 4.2 was used to calculate the overall efficiency. The results are presented in table 4.4.

	Overall Efficiency	**Absolute Increase**	**Relative Increase**
No nanoparticles	23.61 %	- - -	- - -
d = 100 nm	24.72 %	1.12 %	4.73 %
d = 120 nm	25.31 %	1.71 %	7.23 %
d = 140 nm	24.60 %	1.00 %	4.22 %

Table 4.4: The overall efficiency of a PV cell with and without the addition of spherical Al nanoparticles with different diameters d. With d = 120 nm the efficiency is 1.71 % higher than with no nanoparticles, representing a relative increase of 7.23 %.

All the efficiencies presented in table 4.4 are higher than the efficiency of commercial Si PV cells, which is around 20 %. Taking into account that the above efficiencies are calculated assuming a Si PV cell where the material properties are ideal, a higher efficiency was expected. What is more interesting is comparing the results for the different configurations, as the material properties of the PV cell are the same for all. The introduction

of Al nanoparticles leads to an increase in the efficiency for all three diameters. The increase is largest when adding nanoparticles of diameter 120 nm, which is as expected from the transmission results discussed in section 4.3.

4.5 Material Costs of Aluminum Nanoparticles

The calculation of the material costs with the addition of Al nanoparticles to a PV cell is based on the nanoparticles giving the largest increase in efficiency. Assume Al nanoparticles of diameter 120 nm and period 360 nm in a square array on a 1 m^2 flat PV panel, as illustrated in fig. 4.16. The number of nanoparticles needed can then be found.

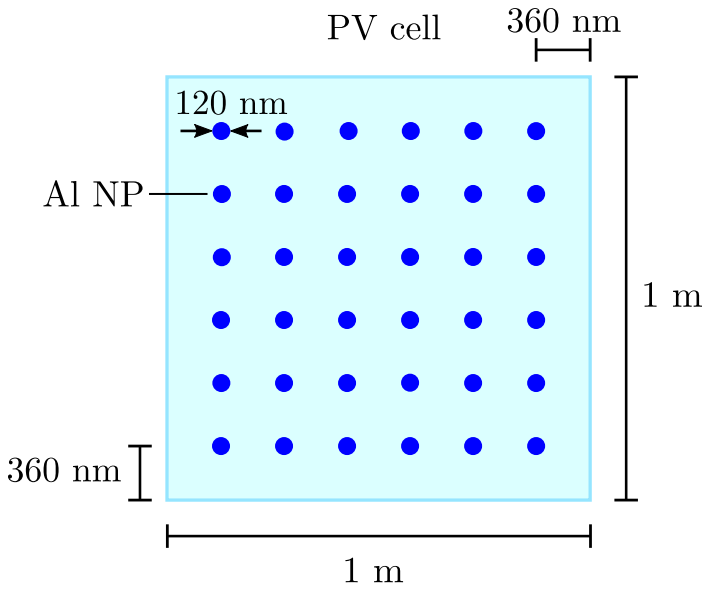

Figure 4.16: The top view of Al nanoparticles in a square array on top of a 1 m^2 PV cell. Not to scale.

First, the number n of nanoparticles along one side is calculated

$$n = \frac{1\text{ m} - 360 \cdot 10^{-9}\text{ m}}{360 \cdot 10^{-9}\text{ m}} \approx 2,777,777 \tag{4.3}$$

The total number N of nanoparticles needed on a 1 m^2 PV panel is then

$$N = n^2 = 7.716 \cdot 10^{12} \tag{4.4}$$

This gives a total volume V of all the nanoparticles

$$V = N \cdot \frac{4\pi r^3}{3} = 6.981 \cdot 10^{-9}\text{ m}^3 \tag{4.5}$$

The density ρ of Al is 2700 kg/m^3 [61]. Thus, the total mass M of Al necessary to add Al nanoparticles of diameter 120 nm and period 360 nm on top of a 1 m^2 PV cell is

$$M = \rho V = 1.885 \cdot 10^{-5} \text{ kg} \tag{4.6}$$

At Sigma-Aldrich, 1 kg of ReagentPlus® Al beads, size 5-15 mm, 99.9 % trace metals basis, costs 2,180.00 NOK. The material costs c of the Al nanoparticles are then

$$c = M \cdot 2,180.00 \text{ NOK} = 0.0411 \text{ NOK} \tag{4.7}$$

This is a very low cost. However, this is only the material costs. Both the synthesizing and deposition of the nanoparticles onto the PV cell surface will give additional costs.

4.6 Summary of Results

The main simulations in this thesis were the simulations with spherical Al nanoparticles of various diameters on top of a Si_3N_4 coated Si slab under angled illumination. However, before these simulations could take place, a parameter space for the simulations had to be selected, and the initial simulations determined the thickness of the oxide layer on the Al nanoparticles and the period. All oxide thicknesses gave an increase in transmission, but the increase was largest with a 3 nm oxide, which, very conveniently, is a native oxide thickness (see fig. 4.8). When simulating with different periods it was seen that the period had to be twice as large as the nanoparticle diameter to avoid near-field effects between the nanoparticles. However, if the period was larger than three times the diameter of the nanoparticles a decrease in transmission at some wavelengths was seen due to far-field coupling via diffraction. The period was therefore chosen to be three times the diameter of the nanoparticles, where the transmission with nanoparticles was higher than or equal to the transmission with no nanoparticles at all wavelengths (see fig. 4.5).

The simulations with spherical Al nanoparticles under angled illumination all gave promising results. When adding Al nanoparticles with diameters 100 nm the transmission over all angles (0 to 55°) and wavelengths (400 to 900 nm) increased by 4.93 % which resulted in an overall PV cell efficiency increase of 1.12 % and a relative increase of 4.73 %. The increase in transmission was largest (8.52 %) for an incident light angle of 5°. The addition of Al nanoparticles with diameters 120 nm gave an increase in transmission of 7.46 % over all angles and wavelengths and resulted in an overall PV cell efficiency increase of 1.71 % and a relative increase of 7.23 %. The increase was largest (12.73 %) for light at normal incidence. When Al nanoparticles with diameter 140 nm were added the transmission over all angles and wavelengths increased by 4.65 % and the overall PV cell efficiency increased by 1.00 %. The relative increase in the overall efficiency was 4.22 %. The increase in transmission was again largest (12.86 %) for light at normal incidence (see tables 4.2, 4.3 and 4.4).

In summary, the addition of 120 nm in diameter Al nanoparticles gave the highest transmission and overall efficiency of the PV cell. Note that the transmission is highest for normal incident light, thus making the addition of nanoparticles to PV cells an interesting alternative not only in areas with diffuse light conditions, but also in areas with direct light

conditions. The abundance of Al and the fact that the material costs of Al nanoparticles are very low makes the results even more interesting.

Simulations with Al nanodisks were also done to see if planar fabricated nanodisks could be used. First, simulations were done to determine the period and height of the nanodisks. The period was three times larger than the diameter of the nanoparticles and the height was 15 nm. Thereafter, simulations where the diameter of the nanodisks and incident light angle varied were done. All diameters (40, 80 and 120 nm) resulted in a decrease in transmission into the Si. Thus, it is not suitable to add Al nanodisks on top of a Si PV cell to decrease the reflection off of the surface.

4.6.1 Simulations: Open Questions

There are some open questions regarding the simulation results.

- When reproducing results from the literature in section 4.2.2, the original and reproduced results are well overlapping in the wavelength interval 400 to 1200 nm. However, from 300 to 400 nm, the reproduced results show a very low transmission compared to the original results. The reason for this reduction is not clear. It could be due to a difference in some of the simulation parameters, such as the placement of the monitor measuring the transmission and the Al material chosen from Lumerical's database.

- In section 4.2.5 there is a characteristic feature in the simulation results for p-polarized light when illuminating with an incident light angle steeper than 25°. The feature occurs at the same wavelength for all nanoparticle diameters and red-shifts as the angle increases. Thus, it seems like what happens depends on the wavelength and incident angle of the light as well as the polarization of the light, and not the nanoparticle diameter. Why this feature occurs is not clear.

Chapter 5

Results and Discussion - Experiments

In this chapter, results from experiments are presented and discussed. First, the experimental results of the experiments done at the Department of Physics and Technology (IFT) are presented, before the experiments done or planned to be done at Rice University are presented.

5.1 Experiments Done at IFT

5.1.1 Characterization of the Photovoltaic Solar Cells

Originally it was planned to do experiments using commercial silicon (Si) PV cells provided by IFE, and thus as a first step, these samples were characterized. It was later decided to simplify the experiments and do measurements and simulations on flat substrates. However, these initial experiments on structured surfaces are included here for future reference.

As a first step, the surface of the PV cells from IFE was imaged using both scanning electron microscopy (SEM) and atomic force microscopy (AFM). Fig. 5.1 shows SEM images of the PV cell surface and fig. 5.2 shows a 3D image of the same surface, generated from an AFM image in the software Gwyddion [62]. The images clearly illustrate the pyramidal structure of the surface, as explained in section 1.4.1.

Fig. 5.3 shows the IV characteristics of one of the PV cells from IFE. The path is typical for a PV cell, which shows that the PV cells worked as they should (see section 2.1.3). The voltage scale is inverted due to how the electrodes were coupled to the potentiostat.

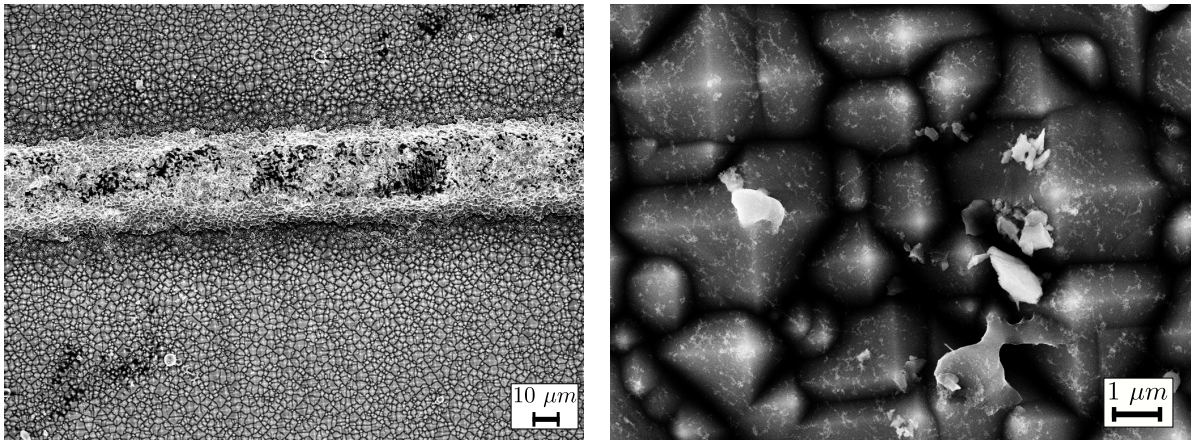

(a) (b)

Figure 5.1: SEM images of the PV cells used. a) Image of the structured PV cell surface and the finger. b) Image of the structured PV cell surface with higher magnification. The image shows some defects.

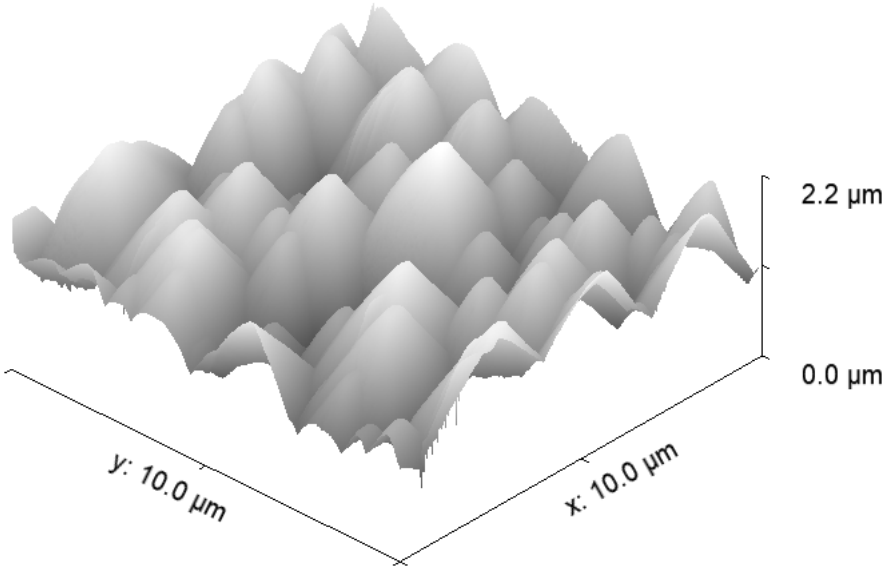

Figure 5.2: AFM generated image of the PV cells used. The pyramids have random height, and is as high as 2.2 μm at this site.

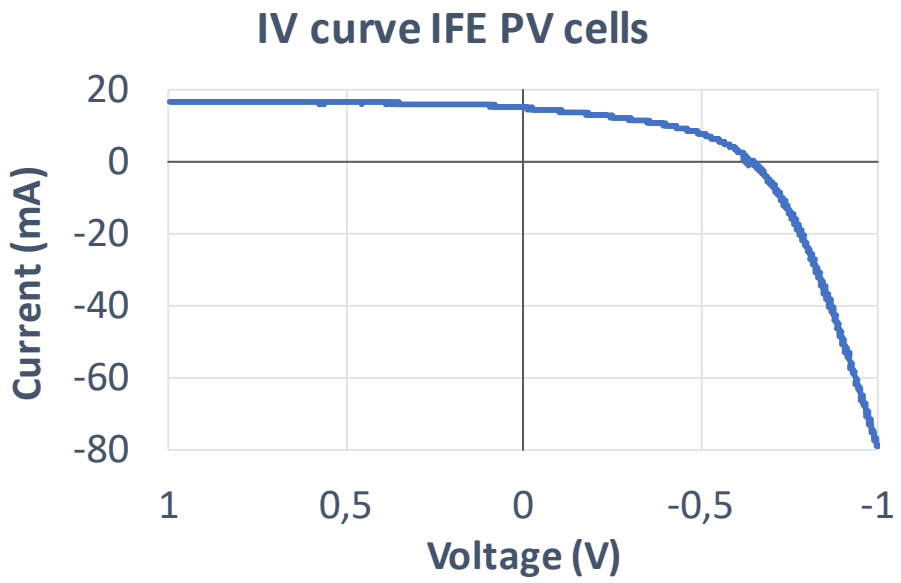

Figure 5.3: The IV characteristics of one of the PV cells from IFE, showing the typical path of a PV cell. This means that the PV cell worked.

5.2 Experiments Planned/Done at Rice University

5.2.1 Deposition of Silicon Nitride on Silicon Dioxide Wafers

Samples for the transmission measurements had to be prepared. As described in section 3.3.1, the sputtering system was to be used to deposit a 160 nm thin film of silicon nitride (SiN_x) on a silicon dioxide (SiO_2) wafer. Then, the thickness of the film should be confirmed using the ellipsometer. The deposition was tried once by reactive sputtering using a Si target and a mix of nitrogen (N) and argon (Ar) gas, but when the thickness was measured with the ellipsometer the film was too thick. It was therefore decided to wait for the silicon nitride (Si_3N_4) target and do regular sputtering using this target. However, the stay at Rice University was terminated before the target arrived.

5.2.2 Transmission Measurements With and Without Nanoparticles

When the samples were ready, the plan was to deposit aluminum (Al) nanoparticles on top of the SiN_x layer and do transmission measurements using a microscope. To get angled illumination, condensers of various NA together with a dark-field insert into the beam path were to be used. The microscope was connected to a computer from which the transmission could be read.

5.2.3 Dark-Field Scattering

The dark-field microscope was used both to obtain scattering measurements of single Al nanoparticles on top of a flat silicon nitride (Si_3N_4) coated (83 nm) Si surface and to do dark-field scattering measurements of the structured PV cells from IFE. Then, it was planned to continue with scattering measurements of the structured PV cell surface while slowly adding Al nanoparticles and see if there was a change. This could not be completed since Rice University closed due to the COVID-19 pandemic. However, after the stay at Rice University was terminated, Christian Jacobsen, a researcher at Rice University, did some dark-field scattering measurements before the university closed.

Figs. 5.4 and 5.5 shows the scattering spectra of Al nanoparticles with diameters 130 and 153 nm, respectively, located on top of a flat Si_3N_4 coated Si surface, together with SEM images of the nanoparticles. These measurements were done to get a better understanding of how the nanoparticles interact with light. The smallest particle (fig. 5.4) resonates at approximately 4 eV, corresponding to 310 nm. The resonance of the largest particle (fig. 5.5) is slightly red-shifted to approximately 3.8 eV, corresponding to 326 nm.

The scattering in the wavelength region giving the highest transmission in the simulations, 400 to 600 nm, which corresponds to 2 to 3 eV, is small for both nanoparticles. However, the scattering spectra measured using the dark-field microscope does not include any forward scattering, and it is therefore hard to tell from these measurements how the addition of these nanoparticles to the PV cell would impact the transmission of light into the cell. Anyhow, the backward scattering in this region is small.

Both nanoparticle resonances are slightly blue-shifted compared to the spectral position of the scattering cross section resonance of the Al nanoparticles in the simulations (see section 4.2.1), which ranged from 340 to 400 nm, increasing with size. However, as is clear from the SEM images of the nanoparticles, the nanoparticles are not perfectly spherical, which is the case for the nanoparticles in the simulations. Besides, the dark-field scattering only includes part of the scattered field from the nanoparticles, as already mentioned. Both these aspects will impact the spectral position of the resonance in the scattering.

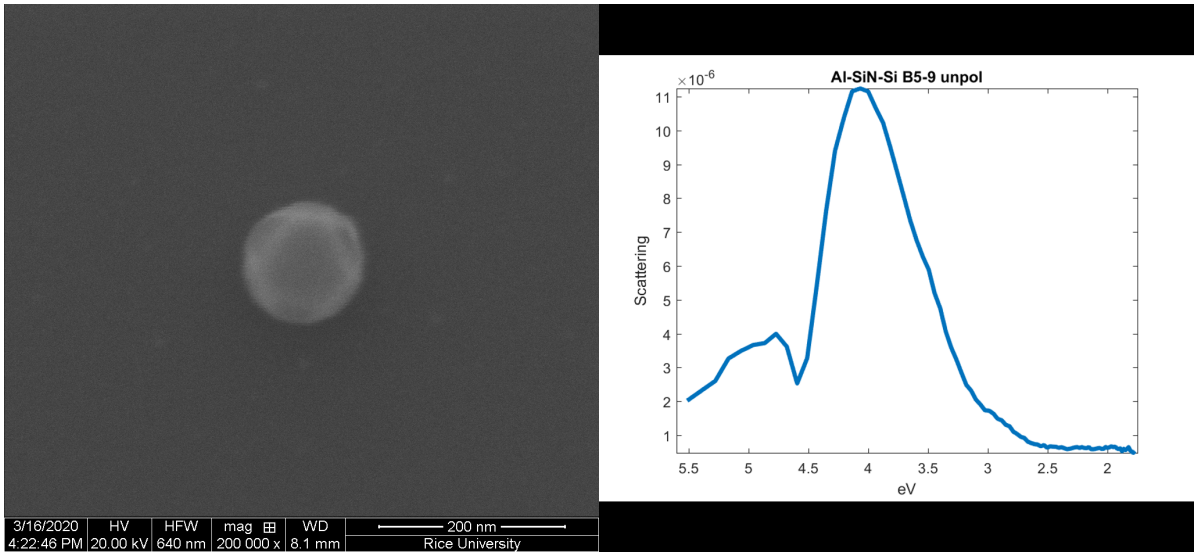

Figure 5.4: SEM image and dark-field scattering spectra of an Al nanoparticle with diameter 130 nm.

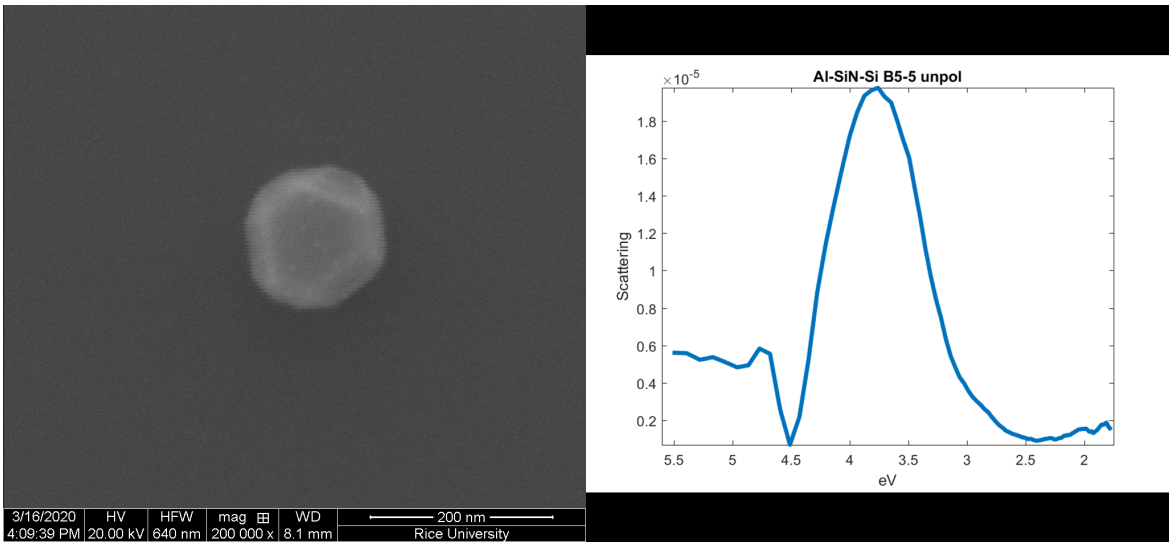

Figure 5.5: SEM image and dark-field scattering spectra of an Al nanoparticle with diameter 153 nm.

Dark-field scattering measurements of the structured PV cell surface from IFE are presented in fig. 5.6. The scattering off of the PV cell is in arbitrary units and is a function of energy/wavelength. It is clear that the scattering off of the PV cell surface peaks in the blue - near-UV spectral region, at around 350 nm. Light in this region has sufficient energy to be absorbed by Si, and it is therefore favorable to reduce the scattering off of the cell surface here. Note that the scattering is still high at 400 to 500 nm, where the increase in transmission with the addition of Al nanoparticles is large. The intensity of the solar spectrum, both direct and diffuse, is also high in this region, making it important to reduce the scattering off of the PV cell here.

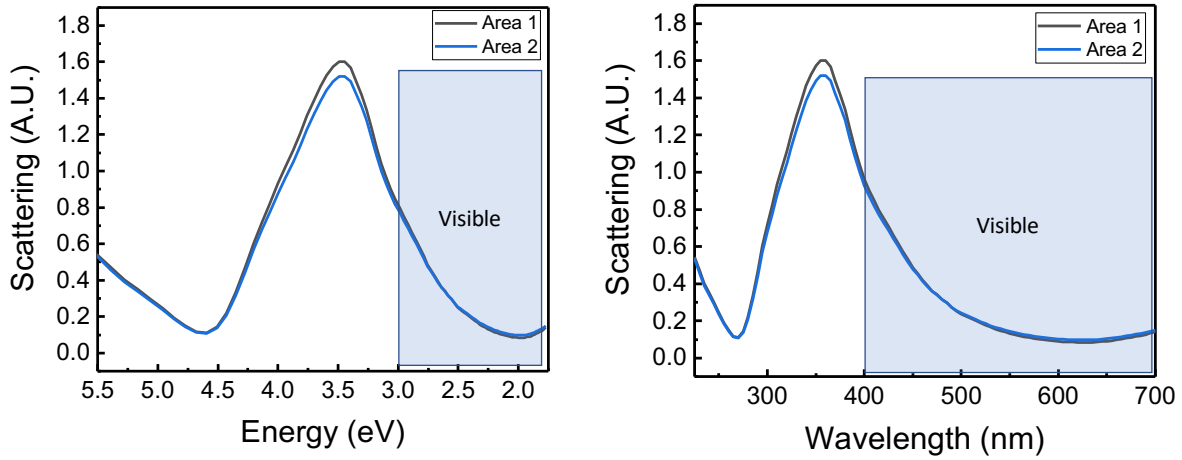

(a) (b)

Figure 5.6: The scattering spectra off of two different areas of a structured PV cell from IFE as a function of a) energy and b) wavelength.

Chapter 6

Conclusion and Suggestions for Future Work

In this thesis, the objective has been to investigate how plasmonic nanoparticles can be used to improve the efficiency of commercial silicon (Si) PV cells under diffuse light conditions. Through simulations, the transmission of light into flat Si PV cells under angled illumination has been studied. The simulation results show a significant increase in light transmitted into the PV cell by the addition of natively oxidized spherical aluminum (Al) nanoparticles on top of the PV cell.

When deciding on which nanoparticle material to use, not only the increase in efficiency of the PV cell by the addition of the nanoparticles has been considered. It has also been of importance to select a material that will be sustainable in large scale production. Thus, abundance have been emphasized. These aspects lead to selecting Al with a 3 nm oxide layer as the nanoparticle material. Al is an abundant and cheap material and spherical Al nanoparticles have shown promising effects in plasmonic PV cells previously.

Initial simulations were done to optimize the period of the Al nanoparticles and the thickness of the oxide layer on them. These simulations showed that the period affected the transmission of light into the PV cell negatively if it was not at least twice the diameter of the nanoparticles due to near-field effects. However, a period four times the diameter also gave a reduction in transmission at some wavelengths. The period was therefore chosen to be three times the diameter of the nanoparticles. The thickness of the oxide layer also affected the transmission of light into the PV cell. The thinner oxide layer, 3 nm, gave the highest transmission, but the introduction of fully oxidized Al nanoparticles also gave an increase in transmission compared to a bare PV cell.

When simulating the transmission of light into the PV cell under angled illumination where Al nanoparticles of diameters 100, 120 and 140 nm with a 3 nm oxide layer were added, there was an increase in transmission for all nanoparticle sizes. The largest increase was for the nanoparticles with a diameter of 120 nm, which gave an increase in transmission of 7.46 % over all wavelengths and angles. Assuming a Si PV cell with ideal material properties, this increase in transmission leads to an increase in the overall PV cell efficiency of 7.23 %, or an absolute increase of 1.71 %, compared to a bare Si PV cell of the same material.

The results from the simulations are very promising, but they need to be further investigated. Due to the outbreak of the COVID-19 pandemic, experiments based on the simulation results could not be performed. In the future, experiments where Al nanoparticles with a 3 nm oxide layer are added on Si PV cells need to be performed.

In conclusion, the addition of spherical Al nanoparticles in the diameter range 100 to 140 nm with a 3 nm oxide layer on top of a Si PV cell has given very promising results and needs to be investigated further. A theoretical publication presenting the simulation results from this thesis work is currently in preparation.

Bibliography

[1] J. F. B. Mitchell. The "Greenhouse" effect and climate change. *Reviews of Geophysics*, 27(1):115–139, 1989.

[2] T. F. Stocker, D. Qin, G.-K. Plattner, and others (eds.). IPCC, 2013: Climate Change 2013: The Physical Science Basis. Contribution of Working Group I to the Fifth Assessment Report of the Intergovern- mental Panel on Climate Change, 2013.

[3] B. Dudley et al. BP Statistical Review of World Energy 2019. `https://www.bp.com/content/dam/bp/business-sites/en/global/corporate/pdfs/energy-economics/statistical-review/bp-stats-review-2019-full-report.pdf`, June 2019.

[4] IEA (2019). IEA World Energy Outlook 2019. `https://www.iea.org/reports/world-energy-outlook-2019`, 2019.

[5] DNV-GL. Energy Transition Outlook 2019, Executive Summary, 2019.

[6] United Nations. Paris Agreement. `https://unfccc.int/files/essential_background/convention/application/pdf/english_paris_agreement.pdf`, 2016.

[7] R. L. Jaffe and W. Taylor. *The Physics of Energy*. Cambridge University Press, 2018.

[8] G. Masson, I. Kaizuka, et al. Trends In Photovoltaic Applications 2019, 2019.

[9] M. Di Vece. Using Nanoparticles as a Bottom-up Approach to Increase Solar Cell Efficiency. *KONA Powder and Particle Journal*, advpub, 2019.

[10] P. A. Lynn. Electricity from Sunlight: An Introduction to Photovoltaics, 2010.

[11] C. Gueymard. *SMARTS2, a simple model of the atmospheric radiative transfer of sunshine: algorithms and performance assessment*. 01 1995.

[12] NVE. Vannkraft. `https://www.nve.no/energiforsyning/kraftproduksjon/vannkraft/?ref=mainmenu`, 2020.

[13] NRK and Meteorologisk institutt. Her regner det 200 dager i året. `https://www.yr.no/artikkel/her-regner-det-200-dager-i-aret-1.14485816`, March 2019.

[14] F. Enrichi, A. Quandt, and G. C. Righini. Plasmonic enhanced solar cells: Summary of possible strategies and recent results. *Renewable and Sustainable Energy Reviews*, 82:2433 – 2439, 2018.

[15] P. Papet, O. Nichiporuk, A. Kaminski, Y. Rozier, J. Kraiem, J.-F. Lelievre, A. Chaumartin, A. Fave, and M. Lemiti. Pyramidal texturing of silicon solar cell with TMAH chemical anisotropic etching. *Solar Energy Materials and Solar Cells*, 90(15):2319 – 2328, 2006. Selected Papers from the Solar Cells and Solar Energy Materials Symposium -IMRC 2005.

[16] C. R. Baraona and H. W. Brandhorst. Proc. 11th Photovoltaic Specialists' Conf. P Phoenix, AZ. page 44. IEEE, New York (1975), May 6-8 1975.

[17] B. L. Sopori. Reflection characteristics of textured polycrystalline silicon substrates for solar cells. *Solar Cells*, 25(1):15 – 26, 1988.

[18] A. V. Narasimha Rao, V. Swarnalatha, A. K. Pandey, et al. Determination of precise crystallographic directions on Si{111} wafers using self-aligning pre-etched pattern. *Micro and Nano Systems Letters*, 6(4), 2018.

[19] E. Vazsonyi, K. De Clercq, R. Einhaus, E. Van Kerschaver, K. Said, J. Poortmans, J. Szlufcik, and J. Nijs. Improved anisotropic etching process for industrial texturing of silicon solar cells. *Solar Energy Materials and Solar Cells*, 57(2):179 – 188, 1999.

[20] P. Campbell and M. A. Green. Light trapping properties of pyramidally textured surfaces. *Journal of Applied Physics*, 62(1):243–249, 1987.

[21] A. McEvoy, T. Markvart, and L. Castaner. *Practical Handbook of Photovoltaics: Fundamentals and Applications*. Elsevier Science & Technology, San Diego, 2 edition, 2012.

[22] B. M. Phillips and P. Jiang. Chapter 12 - Biomimetic Antireflection Surfaces. In Akhlesh Lakhtakia and Raúl J. Martín-Palma, editors, *Engineered Biomimicry*, pages 305 – 331. Elsevier, Boston, 2013.

[23] L. G. Coppel. 19 - Theory, Modeling, and Simulation of Printing. In J. Izdebska and S. Thomas, editors, *Printing on Polymers*, pages 307 – 327. William Andrew Publishing, 2016.

[24] P. Campbell. Light trapping in textured solar cells. *Solar Energy Materials*, 21(2):165 – 172, 1990.

[25] K. Luke, Y. Okawachi, M. R. E. Lamont, A. L. Gaeta, and M. Lipson. Broadband mid-infrared frequency comb generation in a Si3N4 microresonator. *Opt. Lett.*, 40(21):4823–4826, November 2015.

[26] K. R. Catchpole and A. Polman. Design principles for particle plasmon enhanced solar cells. *Applied Physics Letters*, 93(19):191113, 2008.

[27] Y. Zhang, B. Cai, and B. Jia. Ultraviolet Plasmonic Aluminium Nanoparticles for Highly Efficient Light Incoupling on Silicon Solar Cells. *Nanomaterials*, 6:95, 05 2016.

[28] P. Yu, F. Zhang, Z. Li, Z. Zhong, A. Govorov, L. Fu, H. Tan, C. Jagadish, and Z. Wang. Giant optical pathlength enhancement in plasmonic thin film solar cells using core-shell nanoparticles. *Journal of Physics D: Applied Physics*, 51(29):295106, June 2018.

[29] T. Soga. Chapter 1 - Fundamentals of Solar Cell. In Tetsuo Soga, editor, *Nanostructured Materials for Solar Energy Conversion*, pages 3 – 43. Elsevier, Amsterdam, 2006.

[30] P. Hofmann. *Solid State Physics: An Introduction*. John Wiley & Sons, Incorporated, 2015.

[31] J. Andrews and N. Jelley. *Energy Science: Principles, Technologies, and Impacts*. Oxford University Press, 2017.

[32] P. G. V. Sampaio and M. O. A. González. Photovoltaic solar energy: Conceptual framework. *Renewable and Sustainable Energy Reviews*, 74(C):590–601, 2017.

[33] P. G. Kik and M. L. Brongersma. *Surface Plasmon Nanophotonics*, pages 1–9. Springer Netherlands, Dordrecht, 2007.

[34] S. A. Maier. *Plasmonics: Fundamentals and applications*. Springer US, 2007.

[35] M. Pelton and G. W. Bryant. *Introduction to Metal-Nanoparticle Plasmonics*. John Wiley & Sons, Incorporated, 2013.

[36] W. A. Murray and W. L. Barnes. Plasmonic Materials. *Advanced Materials*, 19(22):3771–3782, 11 2007.

[37] C. F. Bohren and D. R. Huffman. *Particles Small Compared with the Wavelength*, chapter 5, pages 130–157. John Wiley & Sons, Ltd, 2007.

[38] V. Juvé, M. F. Cardinal, A. Lombardi, P. Crut, A.and Maioli, J. Pérez-Juste, L. M. Liz-Marzán, N. Del Fatti, and F. Vallée. Size-Dependent Surface Plasmon Resonance Broadening in Nonspherical Nanoparticles: Single Gold Nanorods. *Nano Letters*, 13(5):2234–2240, 2013. PMID: 23611370.

[39] W. Rechberger, A. Hohenau, A. Leitner, J. Krenn, B. Lamprecht, and F. R. Aussenegg. Optical Properties of Two Interacting Gold Nanoparticles. *Optics Communications*, 220:137–141, 05 2003.

[40] B. Lamprecht, G. Schider, R. T. Lechner, H. Ditlbacher, J. Krenn, A. Leitner, and F. Aussenegg. Metal Nanoparticle Gratings: Influence of Dipolar Particle Interaction on the Plasmon Resonance. *Physical Review Letters*, 84:4721, 06 2000.

[41] C. F. Bohren. *Absorption and scattering of light by small particles*. Wiley-VCH Verlag GmbH & Co. KGaA, Weinheim, Germany, 2004.

[42] Lumerical Inc. Finite Difference Time Domain (FDTD) solver introduction. https://support.lumerical.com/hc/en-us/articles/360034914633-Finite-Difference-Time-Domain-FDTD-solver-introduction, 2019.

[43] B. Liang, M. Bai, H. Ma, N. Ou, and J. Miao. Wideband Analysis of Periodic Structures at Oblique Incidence by Material Independent FDTD Algorithm. *IEEE transactions on antennas and propagation*, 2014.

[44] Lumerical Inc. Broadband Fixed Angle Source Technique (BFAST). https://support.lumerical.com/hc/en-us/articles/360034902273-Broadband-Fixed-Angle-Source-Technique-BFAST-, 2019.

[45] ThorLabs. OSL1, OSL1-EC, High Intensity Fiber Light Source, Operating Manual. https://www.thorlabs.de/drawings/ecd5e83f4b3b06e3-02F67D7D-EB2D-FF24-7C576CBB5EFA7034/OSL1-EC-Manual.pdf, 2011.

[46] Rice SEA. https://sea.rice.edu/instruments/cleanroom-facilities, May 2020.

[47] S. Swann. Magnetron sputtering. *Physics in Technology*, 19(2):67–75, mar 1988.

[48] G. Bräuer. 4.03 - Magnetron Sputtering. In Saleem Hashmi, Gilmar Ferreira Batalha, Chester J. [Van Tyne], and Bekir Yilbas, editors, *Comprehensive Materials Processing*, pages 57 – 73. Elsevier, Oxford, 2014.

[49] V.-M. Airaksinen. Chapter 15 - Silicon Wafer and Thin Film Measurements. In Markku Tilli, Teruaki Motooka, Veli-Matti Airaksinen, Sami Franssila, Mervi Paulasto-Kröckel, and Veikko Lindroos, editors, *Handbook of Silicon Based MEMS Materials and Technologies (Second Edition)*, Micro and Nano Technologies, pages 381 – 390. William Andrew Publishing, Boston, second edition, 2015.

[50] H. Wang and P. K. Chu. Chapter 4 - Surface Characterization of Biomaterials. In Amit Bandyopadhyay and Susmita Bose, editors, *Characterization of Biomaterials*, pages 105 – 174. Academic Press, Oxford, 2013.

[51] M. J. McClain, A. E. Schlather, E. Ringe, N. S. King, L. Liu, A. Manjavacas, M. W. Knight, I. Kumar, K. H. Whitmire, H. O. Everitt, P. Nordlander, and N. J. Halas. Aluminum Nanocrystals. *Nano Letters*, 15(4):2751–2755, 2015. PMID: 25790095.

[52] D. Chattopadhyay. Endangered elements of the periodic table. *Resonance*, 22:79–87, 02 2017.

[53] L. C. Hirst, M. K. Yakes, J. H. Warner, M. F. Bennett, K. J. Schmieder, R. J. Walters, and P. P. Jenkins. Intrinsic radiation tolerance of ultra-thin GaAs solar cells. *Applied Physics Letters*, 109(3):033908, 2016.

[54] W. F. McDonough and S.-S. Sun. The composition of the Earth. *Chemical Geology*, 120(3):223 – 253, 1995. Chemical Evolution of the Mantle.

[55] S. Ghanta and K. Muralidharan. Chemical synthesis of aluminum nanoparticles. *Journal of Nanoparticle Research*, 15, June 2013.

[56] M. J. McClain, A. E. Schlather, E. Ringe, N. S. King, L. Liu, A. Manjavacas, M. W. Knight, I. Kumar, K. H. Whitmire, H. O. Everitt, P. Nordlander, and N. J. Halas. Aluminum Nanocrystals. *Nano Letters*, 15(4):2751–2755, 2015. PMID: 25790095.

[57] E. D. Palik and G. Ghosh. *Handbook of Optical Constants of Solids, Five-Volume Set: Handbook of Thermo-Optic Coefficients of Optical Materials with Applications*, volume 1. Academic Press, 1997.

[58] D. E. Aspnes and A. A. Studna. Dielectric functions and optical parameters of Si, Ge, GaP, GaAs, GaSb, InP, InAs, and InSb from 1.5 to 6.0 ev. *Phys. Rev. B*, 27:985–1009, Jan 1983.

[59] R. M. Metzger. Solid-State Physics. In *The Physical Chemist's Toolbox*, pages 443–502. John Wiley & Sons, Inc., Hoboken, NJ, USA, 2012.

[60] National Renewable Energy Lab. Reference Air Mass 1.5 Spectra. `https://www.nrel.gov/grid/solar-resource/spectra-am1.5.html`, March 2020.

[61] C. J. (Colin James) Smithells. Smithells metals reference book, 2004.

[62] D. Nečas and P. Klapetek. Gwyddion: an open-source software for SPM data analysis. *Central European Journal of Physics*, 10:181–188, 2012.